Ubiquitination of DNA damage-stalled RNAPII promotes transcription-coupled repair

Yuka Nakazawa[1, 2], Yuichiro Hara[1, 2, 17], Yasuyoshi Oka[1, 2, 17], Okiru Komine[3, 4, 17], Diana van den Heuvel[5, 17], Chaowan Guo[1, 2, 17], Yasukazu Daigaku[6, 7, 17], Mayu Isono[1, 2], Yuxi He[1, 2], Mayuko Shimada[1, 2], Kana Katoh[1, 2], Nan Jia[1, 2], Satoru Hashimoto[1, 2], Yuko Kotani[8, 9], Yuka Miyoshi[3, 4], Miyako Tanaka[10, 11], Akira Sobue[3, 4], Norisato Mitsutake[12], Takayoshi Suganami[10, 11], Akio Masuda[13], Kinji Ohno[13], Shinichiro Nakada[14, 15], Tomoji Mashimo[8, 9, 16], Koji Yamanaka[3, 4], Martijn S. Luijsterburg[5], Tomoo Ogi[1, 2, 18, *]

[1]Department of Genetics, Research Institute of Environmental Medicine (RIeM), Nagoya University, Nagoya, Japan
[2]Department of Human Genetics and Molecular Biology, Graduate School of Medicine, Nagoya University, Nagoya, Japan
[3]Department of Neuroscience and Pathobiology, Research Institute of Environmental Medicine (RIeM), Nagoya University, Nagoya, Japan
[4]Department of Neuroscience and Pathobiology, Graduate School of Medicine, Nagoya University, Nagoya, Japan
[5]Department of Human Genetics, Leiden University Medical Center (LUMC), Leiden, The Netherlands
[6]Frontier Research Institute for Interdisciplinary Sciences, Tohoku University, Sendai, Japan
[7]Graduate School of Life Sciences, Tohoku University, Sendai, Japan
[8]Institute of Experimental Animal Sciences, Graduate School of Medicine, Osaka University, Osaka, Japan
[9]Genome Editing Research and Development (R&D) Center, Graduate School of Medicine, Osaka University, Osaka, Japan
[10]Department of Molecular Medicine and Metabolism, Research Institute of Environmental Medicine (RIeM), Nagoya University, Nagoya, Japan
[11]Department of Immunometabolism, Graduate School of Medicine, Nagoya University, Nagoya, Japan
[12]Department of Radiation Medical Sciences, Atomic Bomb Disease Institute , Nagasaki University, Nagasaki, Japan
[13]Division of Neurogenetics, Center for Neurological Diseases and Cancer, Nagoya University Graduate School of Medicine, Nagoya, Japan
[14]Department of Bioregulation and Cellular Response, Graduate School of Medicine, Osaka University, Osaka, Japan
[15]Institute for Advanced Co-Creation Studies, Osaka University, Osaka, Japan
[16]Division of Animal Genetics, Laboratory Animal Research Center, Institute of Medical Science, The University of Tokyo

[17]These authors contributed equally to this work.
[18]Lead contact: T.O. (togi@riem.nagoya-u.ac.jp)
[*]Corresponding author: T.O. (togi@riem.nagoya-u.ac.jp)

Summary (150 words)

Transcription-coupled nucleotide excision repair (TC-NER) is initiated by the stalling of elongating RNA polymerase II (RNAPIIo) at DNA lesions. The ubiquitination of RNAPIIo in response to DNA damage is an evolutionarily conserved event, but its function in mammals is unknown. Here, we identified a single DNA damage-induced ubiquitination site in RNAPII at RPB1-K1268, which regulates transcription recovery and DNA damage resistance. Mechanistically, RPB1-K1268 ubiquitination stimulates the association of the core-TFIIH complex with stalled RNAPIIo through a transfer mechanism that also involves UVSSA-K414 ubiquitination. We developed a strand-specific ChIP-seq method, which revealed RPB1-K1268 ubiquitination is important for repair and the resolution of transcriptional bottlenecks at DNA lesions. Finally, RPB1-K1268R knock-in mice displayed a short life-span, premature ageing, and neurodegeneration. Our results reveal RNAPII ubiquitination provides a two-tier protection mechanism by activating TC-NER and, in parallel, the processing of DNA damage-stalled RNAPIIo, which together prevent prolonged transcription arrest and protect against neurodegeneration.

Introduction

The timely expression of genetic information is crucial for life. However, genomic DNA is continuously damaged, and unrepaired DNA lesions interfere with transcription (Jackson and Bartek, 2009). Eukaryotic cells preferentially remove DNA lesions from the transcribed strand of active genes by transcription-coupled nucleotide excision repair (TC-NER) (Hanawalt and Spivak, 2008). By preventing prolonged stalling of RNA polymerase II (RNAPII) at DNA lesions (Brueckner et al., 2007), TC-NER ensures swift transcription recovery and avoids apoptosis. Individuals suffering from Cockayne syndrome (CS) have defective TC-NER due to mutations in either the *CSA*/*ERCC8* or the *CSB*/*ERCC6* gene, and display developmental abnormalities, premature ageing and progressive neurodegeneration (Laugel, 2013). These CS clinical features are likely caused by transcriptional misregulation of certain genes (Wang et al., 2014), and cytotoxicity associated with prolonged stalling of RNAPII (Ljungman and Zhang, 1996; Marteijn et al., 2014; Reid-Bayliss et al., 2016; Yamaizumi and Sugano, 1994).

TC-NER is triggered by the stalling of elongating RNAPII molecules (RNAPIIo) at DNA lesions (Xu et al., 2017). The Cockayne syndrome protein complex (CSA/CSB) as well as the UV-sensitive syndrome protein (UVSSA) collaborate in the processing of RNAPIIo and the recruitment of repair factors (Nakazawa et al., 2012; Okuda et al., 2017; van der Weegen et al., 2019). These events trigger the unwinding and excision of the lesion-containing DNA fragment, which is followed by repair synthesis and ligation to complete repair (Aboussekhra et al., 1995). A key event in TC-NER is the recruitment of the TFIIH complex, which is a general transcription factor that also functions in NER. However, it is currently unknown how stalled RNAPIIo molecules transmit a signal to recruit the TFIIH complex to initiate repair and to resume transcription.

One possibility is that the post-translational modification of stalled RNAPIIo is involved in this process. It was indeed described ~20 years ago that the catalytic subunit of RNAPII (RPB1) becomes ubiquitinated in response to DNA damage in both yeast and human cells (Gregersen and Svejstrup, 2018). Extensive studies in yeast *S. cerevisiae* have suggested that the ubiquitination of RPB1 is not required for TC-NER, but rather acts in a last resort pathway that regulates displacement and degradation of DNA damage-stalled RNAPII (Lommel et al., 2000; Nouspikel, 2011; Somesh et al., 2005; Somesh et al., 2007; Woudstra et al., 2002). The last resort pathway acts when TC-NER is not available to allow lesion removal by a slower repair pathway, such as global genome repair (GG-NER) without strand specificity. In humans, the mechanisms involved in the ubiquitination and processing of RNAPII are less well understood. Although several proteins have been linked to RNAPII ubiquitination in human cells (Bregman et al., 1996; Ratner et al., 1998; Nakazawa et al., 2012; Kleiman et al., 2005; Starita et al., 2005; Yasukawa et al., 2008; Anindya et al., 2007), its precise role remains largely unexplored.

In this study, we identify an evolutionarily conserved DNA damage-induced ubiquitination site at K1268 in the RPB1 subunit of human RNAPII; our results reveal that this single RNAPII ubiquitination promotes transcription-coupled repair and protects against neurodegeneration.

Results

RNA polymerase II is predominantly ubiquitinated at lysine 1268 of RPB1 after UV

To identify damage-induced ubiquitination sites in human RPB1, the largest subunit of RNA polymerase II (RNAPII), we performed a SILAC-mass spectrometry (MS) in UV-irradiated wild-type (WT) and TC-NER-deficient Δ*UVSSA* HCT116 cells. From the initial MS analysis, we only detected RPB1 ubiquitination at lysine 1268 (K1268) (**Table S1**). We further performed label-free MS in WT HeLa cells after UV, which revealed additional RPB1 ubiquitination at K1268, K163, K177, K758, K853, and at K1350 (**Table S2**). All of these RPB1 lysine residues have been reported as putative ubiquitination sites under various conditions (Elia et al., 2015). Importantly, we only robustly detected ubiquitination at K1268 in response to a physiological level of UV-induced DNA damage (**Figure 1A**).

We generated 15 site-specific knockin mutants in which a single RPB1 ubiquitinated lysine was mutated to arginine (RPB1-KR mutants; **Figure 1A**) of which 6 sites were identified in our MS, while 9 residues were reported previously (Elia et al., 2015). All KR mutants were successfully generated using CRISPR/Cas9-based gene editing in HeLa cells except for RPB1-K758R (**Table S3**). We next analysed the UV-induced ubiquitination of the RPB1-KR mutants (**Figure 1B**). Importantly, the UV-induced RPB1-IIo upper bands (IIo-Ubi) overlapped with immunoblot staining for conjugated ubiquitin (**Figure S1A**). Moreover, incubation of GFP-tagged RPB1, purified from UV-irradiated HEK293 cells, with the ubiquitin-endoprotease USP2 *in vitro* resulted in loss of the RPB1-IIo upper bands and the appearance of cleaved mono-ubiquitin (**Figure S1B**). These findings demonstrate that these upper-bands truly represent RPB1-IIo ubiquitination (Bregman et al., 1996; Nakazawa et al., 2012). While most RPB1-KR mutants still showed UV-induced RPB1-IIo ubiquitination, this modification was largely lost in RPB1-K1268R cells (**Figure 1B**). Notably, RPB1-IIo ubiquitination was also severely diminished in Δ*CSB*, Δ*CSA*, and in Δ*UVSSA* cells (**Figures 1B**, **S3A**) (Bregman et al., 1996; Nakazawa et al., 2012; Ratner et al., 1998). Collectively, these data indicate that UV-induced RPB1-IIo ubiquitination occurs predominantly at the K1268 residue. Interestingly, the RPB1-K1268 site is highly conserved (**Figure S1C**), and is surface-exposed near to where the downstream DNA enters RNAPIIo during transcription (He et al., 2016; **Figure S1D**).

RPB1-K1268 ubiquitination is essential for transcription recovery and UV resistance

To address the importance of RPB1-IIo ubiquitination, we measured recovery of RNA synthesis (RRS) after UV irradiation, which is a conventional measure of TC-NER activity. While most RPB1-KR mutants exhibited only minor changes, the RPB1-K1268R cells displayed a prominent defect in RRS (**Figures 1C**, **S1E**). Importantly, nascent transcript levels (general transcription) were unchanged (**Figure S1F**) in the RPB1-K1268R cells.

Clonogenic cell survival revealed an increased sensitivity to UV in most of the RPB1-KR mutants, while the RPB1-K1268R cells exhibited the most pronounced UV sensitivity among the mutants (**Figure 1D**). These results indicate that the

ubiquitination of RPB1 at K1268 residue is important for transcription recovery and cell survival after UV-induced DNA damage.

Cullin E3 ligases ubiquitinate RPB1 at K1268 and form K48- and K63-linked ubiquitin chains in response to UV

To gain insight into the molecular events that mediate RPB1-IIo ubiquitination, we inactivated cullin-ring type E3-ligases (CRLs) with neddylation inhibitor, MLN4924 (Soucy et al., 2009). MLN4924 treatment completely abolished the UV-induced RPB1-IIo ubiquitination, demonstrating that CRLs ubiquitinate the RPB1-K1268 residue (**Figure 2A**). MLN4924 treatment also diminished RRS in WT cells, but not in TC-NER-deficient cells (**Figure 2B**), implying that CRLs play a predominant role in the RPB1-IIo ubiquitination associated with TC-NER activity.

We then studied the compositions of ubiquitin chains formed on the RPB1-K1268 residue. Ubiquitin-pulldown assays confirmed the UV-induced ubiquitination of RPB1-IIo was severely reduced in Δ*CSA* HeLa cells, and abolished in RPB1-K1268R cells (**Figure S2A**). These findings indicate that the ubiquitination of RPB1 primarily occurs on K1268 and is partly dependent on CSA. To investigate which specific ubiquitin chains are formed on RPB1-K1268, Ubiquitin-KR mutants (Ub-K6R, -K11R, -K27R, -K29R, -K33R, -K48R, and -K63R) were expressed in WT HEK293 cells and ubiquitin-pulldown was performed (K27R mutant was not included due to poor expression). Interestingly, we noted substantially reduced total UV-induced RPB1 ubiquitination and increased chain termination products when expressing either Ub-K63R or Ub-K48R (**Figure 2C**), suggesting that these ubiquitin linkages are primarily formed on RPB1-K1268. The presence of both K48- and K63-linked polyubiquitin chains were confirmed in GFP- RPB1 precipitates from HEK293 cells, and these were fully dependent on K1268 (**Figure 2D**). Notably, both K48- and K63-linked RPB1 ubiquitin chains were substantially decreased in Δ*CSA* cells (**Figures 2D**). Taken together, these data indicate that CRLs, including CRL^{CSA}, conjugate K48- and K63-linked ubiquitin chains onto RPB1-IIo at K1268 in response to UV.

Ubiquitination of RPB1-K1268 is crucial for the recruitment of TFIIH after UV

We next set out to define the molecular mechanism through which RPB1-K1268 ubiquitination regulates TC-NER. To this end, we monitored the association of TC-NER factors with ubiquitinated RPB1-IIo by chromatin co-immunoprecipitation. In WT HeLa cells, RPB1-IIo interacted with CSB and the CRL^{CSA} complex as well as with major subunits of the general transcription factor IIH (TFIIH) core-complex, and its associated CAK complex in a UV-dependent manner (**Figure 3A**). Intriguingly, while the RPB1-K1268R interacted normally with CS proteins after UV, its interaction with the core-TFIIH and CAK complexes were severely impaired (**Figure 3A**). Indeed, the UV-dependent recruitment of TFIIH to RPB1-IIo was completely abolished in Δ*CSA,* Δ*CSB,* or Δ*UVSSA* cells (**Figures 3B**, **S3A**), consistent with recent results (van der Weegen et al., 2019). Importantly, a UV dose-dependent increase in the TFIIH interaction was observed in WT cells, but not in RPB1-K1268R cells (**Figure 3C**). TFIIH also did not associate with RPB1-K1268R at late time-points after UV, suggesting an impaired rather than a delayed association (**Figure 3D**). Moreover, we detected persistent association of CSB/CSA in the RPB1-K1268R mutant at late time-points after UV, consistent with defective repair (**Figure 3D**). We also noticed that the

UV-dependent TFIIH interaction was mostly preserved in the other RPB1-KR mutants (**Figure S3B**). Of note, the TFIIH interaction required for the RPB1 C-terminal domain (CTD)-Ser5 phosphorylation during transcription initiation was normal in the RPB1-K1268R cells (**Figure S3C**), suggesting that RPB1-K1268 ubiquitination is specifically involved in engaging TFIIH during TC-NER, but not during transcription initiation.

Mono-ubiquitination of UVSSA transfers TFIIH to RNAPIIo during TC-NER

We next sought to address how RPB1-K1268 ubiquitination is mechanistically linked to the recruitment of TFIIH during TC-NER. We focused on UVSSA because it preferentially binds to ubiquitinated RPB1-IIo after UV irradiation (Nakazawa et al., 2012). In WT cells, we detected the association of endogenous UVSSA with RPB1-IIo after UV, but this was abolished in either Δ*CSA* or Δ*CSB* cells. Conversely, Δ*UVSSA* did not affect the association of the CSB/CSA complex with RPB1-IIo (**Figures 3B**, **S3A**).

We noticed a distinct UVSSA 'mono-ubiquitinated' upper-band detected in RPB1-IIo immunoprecipitates after UV (**Figure 3B**). MS analyses revealed that UVSSA mono-ubiquitination occurs mainly at K414 (our unpublished data; Higa et al., 2018). The mono-ubiquitinated UVSSA disappeared in RPB1-IIo immunoprecipitates in HeLa cells lacking the UVSSA-K414 residue (ΔK414; **Figure 3B**). These findings identify K414 as the key mono-ubiquitination site in UVSSA in response to UV. Strikingly, the interaction between UVSSA and RPB1-IIo was significantly reduced in the RPB1-K1268R cells, and this particularly affected the mono-ubiquitinated form of UVSSA (**Figures 3C**, **S3C**). Although difficult to detect, it appeared that general levels of UVSSA-K414 ubiquitination were mostly unaffected in RPB1-K1268R cells. Interestingly, this K414 residue is located within a stretch of acidic residues in the central region of UVSSA (390-430aa), which directly interacts with the core-TFIIH-p62 pleckstrin homology (PH)-domain (Okuda et al., 2017). To specify critical residues in UVSSA that mediate the TFIIH-p62 recruitment to ubiquitinated RPB1-IIo, we generated Δ*UVSSA* HeLa cells stably expressing the UVSSA-K414R, as well as the PH domain-binding site (PHB) mutants (Okuda et al., 2017). The UV-dependent TFIIH-p62 recruitment to RPB1-IIo was severely compromised in *UVSSA*-ΔK414 cells (**Figure 3B**), as well as in UVSSA-K414R cells (**Figure 3E**), indicating that the UVSSA-K414 ubiquitination is important for the TFIIH recruitment. As expected, the UVSSA-PHB mutants also displayed defects in the TFIIH recruitment (**Figure 3E**). Strikingly, while the PH domain-mediated UVSSA-TFIIH interaction was indeed impaired in the UVSSA-PHB mutants, we detected a normal interaction between the UVSSA-K414R mutant and TFIIH-p62 (**Figure S3D**). Importantly, RRS was impaired in all of the UVSSA mutants (**Figure S3E**), showing that the UVSSA-K414 ubiquitination and the TFIIH-p62 interaction are both critical for TC-NER. Notably, RPB1-IIo ubiquitination was restored to the WT level in all these UVSSA mutant cells (**Figure 3E**) despite their TC-NER defect.

These findings indicate that the damage-induced RNAPIIo ubiquitination mainly occurs prior to the recruitment of UVSSA and TFIIH, and that the ubiquitination of UVSSA-K414 is exclusively needed for the efficient transfer of TFIIH from UVSSA to stalled RNAPIIo (**Figure 3F**), which may involve later displacement of p62 by other NER proteins, such as XPG.

Genome-wide ChIP-seq reveals a strong transcription recovery delay in the RPB1-K1268R mutant

To study the consequence of impaired RPB1-K1268 ubiquitination on a genome-wide scale, we employed chromatin immunoprecipitation of RPB1 to capture DNA fragments, which were analysed by next-generation-sequencing (NGS) (ChIP-seq: **Figure 4A**). This enables the quantitative and spatiotemporal mapping of RNAPII in the genome. We performed ChIP-seq in WT and RPB1-K1268R mutant HeLa cells using antibodies against total RPB1, or CTD phosphorylation-specific RPB1 (**Figure 4A**). Without UV irradiation, in agreement with previous reports (Brookes et al., 2012; Odawara et al., 2011; Rahl et al., 2010), CTD-Ser5-phosphorylated RPB1 (RPB1-Ser5) formed two distinct peaks near transcription start sites (TSS), which reflect RNAPII molecules during transcription initiation and promoter-proximal pausing (**Figure 4B**, right panel gray lines). CTD-Ser2-phosphorylated RPB1 (RPB1-Ser2), which represents the elongating form of RNAPII, was distributed throughout gene-bodies and was significantly enriched after transcription end sites (TES) due to post-transcriptional pausing prior to dissociation (**Figure 4B**, left panel gray lines). Total RPB1 ChIP profiles (pan-RPB1) were a composite of RPB1-Ser2 and RPB1-Ser5 features (**Figure S4A**, right panels gray lines). Importantly, all these RNAPII distribution profiles were identical between RPB1-WT and RPB1-K1268R mutant in undamaged cells (**Figures 4B**, **S4A**), demonstrating that RPB1-K1268 ubiquitination does not affect general transcription.

At 3 h after UV, the distribution of RNAPII was comparable between RPB1-WT and RPB1-K1286R, and significantly shifted with increased enrichment near the 3' of TSS concomitant with a reduction at post-transcriptional pausing sites (PTPS) after the TES (**Figure 4B**, green lines). This suggests that fewer RNAPII molecules reach the end of genes due to DNA damage-induced transcription arrest, stalling or pausing, in agreement with previous analyses (Paulsen et al., 2014). Strikingly, while the RNAPII distribution started to shift back at 12 h after UV in WT cells, the RPB1-K1286R mutant showed impaired transcription recovery (**Figure 4C**). These profile differences were also prominent in individual genes (**Figure 4D**). Importantly, TC-NER-deficient cells showed a similar RNAPII distribution to the K1286R mutant at all time-points analysed except 3 h (**Figures S4A**, **S4B**; see arrows in RPB1-Ser2 3h panels), suggesting this reflects the degree of impaired TC-NER.

Strand-specific ChIP-seq identifies RPB1-IIo stalled at DNA damage and demonstrates slow repair kinetics in RPB1-K1268R mutant in most genes

We next sought to establish a new ChIP-seq method measuring genome-wide TC-NER kinetics. This method relies on the principle that a fraction of the DNA fragments prepared after RPB1-Ser2 ChIP contain DNA lesions in the transcribed strand, which caused RNAPIIo to stall in the first place. These DNA lesions will prevent PCR amplification during the generation of NGS libraries. However, the asymmetric structure of the Illumina library adapters (**Figure 4E**, left panel) allows the strand-specific PCR amplification of fragments without DNA damage resulting in the enrichment of reads in the coding (non-transcribed) strands. Indeed, a shift in strand-biased ChIP-seq reads was clearly detected in UV irradiated samples and this strongly correlated with gene orientation (**Figure 4E**, right upper panel).

To estimate gene-by-gene repair kinetics from the strand-biased ChIP-seq data, we calculated the Strand-Specificity Index (SSI), which reflects the degree of remaining DNA damage in transcribed-strands in individual genes (see **STAR Methods**). Transcription arrests at DNA lesions in gene bodies contribute to an increase in the absolute values of SSI (|SSI|), whereas RNAPIIo molecules pause after transcription at the PTPS do not (**Figure 4E**, right upper panel). Plotting the SSI against the read coverage within 'gene bodies' in individual 'active genes' (9,836 genes, **Figure S4C**) revealed a unimodal distribution in undamaged HeLa cells (no strand-bias) (**Figure 4E**, right bottom panel). Conversely, UV irradiation triggers a bimodal SSI distribution due to bidirectional transcription and the stalling of RNAPIIo. Importantly, treating ChIPed DNA fragments from UV-irradiated cells with a DNA repair enzyme mix (preCR, NEB) prior to library preparation fully reverted the bimodal SSI pattern to a unimodal distribution (**Figure 4F**). Thus, the strand specificity is a true consequence of the presence of UV-induced DNA lesions.

We calculated the SSI to evaluate the impact of RPB1-K1286 ubiquitination on DNA repair kinetics in individual genes. In WT cells, SSI plots shifted to a bimodal distribution at 3 h post-UV irradiation, which returned to a unimodal distribution within 12 h, indicating completion of DNA repair within this time-frame in 'most genes' (**Figure 4G**, WT, red). In contrast, the bimodal distribution remained in the RPB1-K1268R mutant up to 12 h after UV, reflecting a significant delay in the genome-wide removal of DNA lesions by TC-NER (**Figure 4G**, K1268R, blue). To further support this conclusion, we calculated the SSI in TC-NER-deficient cells. Importantly, we first confirmed that the RPB1-Ser2 ChIP-seq read depths of individual genes showed a good correlation between biological replicates in all tested cells (**Figure S4D**). Indeed, all of these TC-NER-deficient cells displayed a bimodal distribution of SSI at 12 h after UV, indicating impaired removal of DNA lesions in most genes in these cells (**Figure S4E**).

In conclusion, our genome-wide analysis supports an important role for RPB1-K1268 ubiquitination in TC-NER-mediated clearing of DNA lesions from transcribed-strands of active genes. In principle, this method can also be applied for the detection of genome-wide RNAPII molecules stalled at various types of other transcription-blocking DNA lesions, such as cisplatin and Illudin S.

A detailed TC-NER repair kinetic in the RPB1-K1268R mutant

Our strand-specific ChIP-seq method overcomes known limitations in conventional methods (Mayer et al., 2017) and enable the evalutaion of gene-by-gene repair kinetics. Indeed, analysis of individual genes (see *MCM3* in **Figure 5A**) revealed slower repair kinetics in RPB1-K1268R cells compared to WT.

To extend our gene-by-gene analysis further, we calculated the Recovery index (RI), which represents the progression of DNA lesion removal from transcribed-strands in the entire genome (see **STAR Methods** and **Figure S5A**). To exclude the effects of RNAPII pausing near TSS, TES, and PTPS, from now on we focused on the 'central genic region' in 5,704 active genes. This selection from 5 kb downstream of the TSS to 5 kb upstream of the TES of >20 kb active genes did not affect the RI kinetics (**Figures 5B**, **S5B**). After reaching a maximum at 1 h post-UV irradiation, WT HeLa cells showed a gradual decrease in RI within 12 h indicative of near-complete repair within this time-frame. However, the RI remained high in RPB1-K1268R and TC-NER-deficient cells indicative of incomplete repair (**Figure 5B**). Surprisingly, Δ*CSB* cells

displayed slower repair kinetics compared to the other cells, which possibly reflects slow repair of UV-induced oxidative DNA damage (Menoni et al., 2018). The RPB1-K1268R cells showed significantly impaired TC-NER activity throughout the genome albeit not as strong as complete loss of TC-NER.

As the average transcription speed is estimated to be ~2.5 kb per min and 7 J/m^2 UV irradiation triggers ~1 lesion per 10 kb, it would be expected that all sparsely running RNAPIIo reach DNA lesions within the first ~10 min post-UV irradiation. However, the RI increases in the first 1-3 h, suggesting a slow-down of the transcription elongation rate after UV. The total number of reads did not decline after UV, while the strand bias increased in the first 3 h (**Figure S5C**), indicating that the RI kinetics truly represent progression of DNA lesion removal from transcribed strands.

Spatial distribution of stalled RNAPIIo molecules associated with TC-NER

We next examined the SSI across relative positions in genes. This analysis revealed that DNA lesions were uniformly removed from entire gene bodies in WT cells (**Figures 5C**, **S5D**), suggesting that TC-NER is initiated simultaneously by sparsely running RNAPIIo molecules that stall at DNA lesions. Interestingly, the concordant increase of SSI was observed in all cell types at early time-points post-UV irradiation (**Figure S5D**), suggesting that *de novo* collisions of sparsely running RNAPIIo with DNA damage continuously occurred within 1 h after UV in all cell types, while further stalling continues afterwards in repair-deficient cells.

We next attempted a base-resolution mapping of DNA damage-stalled RNAPIIo. UV irradiation predominantly generates transcription-blocking cyclobutane pyrimidine dimers (CPDs) in DNA (Friedberg et al., 2005). An abundance of mapped reads in the coding strands near A<>A dimers could indeed be successfully detected in WT HeLa cells after UV (**Figure S5E**, solid line), due to the stalled RNAPIIo at UV-induced T-T CPDs in transcribed strands. We further analysed the RNAPIIo stalling at base-resolution in TC-NER-deficient, as well as RPB1-K1268R cells (**Figures 5D**, **S5F**). Interestingly, we noted an asymmetry in the mapped reads near A<>A dimer sites in the coding strand (T<>T DNA damage in the opposite transcribed strands), suggesting increased accumulation of RNAPIIo at the 5' compared to the 3' lesion-proximal region in RPB1-K1268R cells as well as in TC-NER-deficient cells (**Figure 5D**). The increase of reads immediately adjacent to A<>A dimer sites (h_a: peak height at the damage site measured from the 3' baseline) and that of the 5' regions (h_b: height of the 5', 500bp upstream of the damage site, measured from the 3' baseline) in the coding strand were quantified (**Figure 5E**). As h_b reached its maximum at ~1 h after UV in all cell types with a nearly identical profile (**Figure 5E**, dashed lines), this may reflect the 'queueing' of multiple RNAPII molecules at the 5' side of the T<>T dimer due to 'a transcription traffic jam' right behind the RNAPII molecule that is stalled at the DNA lesion. The queue resolved swiftly in WT cells, but persisted in TC-NER-deficient cells as well as in RPB1-K1286R cells, suggesting that RNAPIIo queueing and its resolution is associated with TC-NER activity and the processing of stalled RNAPIIo.

Gene-by-gene repair profiles identify unrepaired genic features in RPB1-K1268R cells

Analysis of SSI in individual genes exhibited a strong correlation between replicates both in WT and RPB1-K1268R cells at early time points (3-6 h) after UV

irradiation in the entire genome (**Figure 6A**).This indicates that the TC-NER activity is not random, but rather reflects a tight coordination between gene-by-gene transcription and repair. This correlation was reduced and stochastic events became more prominent at 12 h after UV, suggesting that random DNA repair by GG-NER dominates over TC-NER at this time-point. Differential read coverage analysis identified genes that were left unrepaired (red dots in **Figure 6A**). These analyses were also performed in TC-NER-deficient cells (**Figure S6A**), which revealed an overlap in the sets of unrepaired genes between cell types (**Figure 6B**). While there was only 20 % overlap between all conditions (WT-KR-ΔTCR), which reflects 'common unrepaired genes' between WT and repair-deficient cell types (KR-ΔTCR), there was about 80% (KR-ΔTCR) overlap between unrepaired genes among the RPB1-K1268R (KR) and TC-NER-deficient (ΔTCR) cells. Within these overlapping genes, (**Figure 6B**), we analysed common features, such as gene length (**Figure 6C**) and GC contents (**Figure 6D**), as well as RPB1 ChIP-seq read density, a proxy to gene expression level (**Figure 6E**) of the individual genes. The common unrepaired genes (WT-KR-ΔTCR, blue) as well as the overlapping genes between the KR and ΔTCR (green) cells were generally long in size, exhibited low-GC content, and low-expression profiles, while genes only detected in the ΔTCR-set (yellow) had no obvious characteristic features to distinguish them from 'promptly repaired' genes (pink, 2,005 genes outside the Venn diagram in **Figure 6B**). Representative unrepaired genes in RPB1-K1268R cells are shown in **Figure 6F**.

We further performed a gene-enrichment analysis on the identified unrepaired genes in RPB1-K1268R that were repaired in WT cells. We detected a significant accumulation of unrepaired genes in the 'cell cycle' pathway (KEGG pathway ID hsa04110, p=5.60×10^{-11}; **Figure S6B**), such as genes encoding CDK-cyclin, ORC, and MCM (see *MCM3* repair profiles in **Figure 5A**) complexes, all of which positively regulate the cell cycle progression. These cell cycle genes are relatively long (median length: cell cycle genes, 36kb; other genes, 22kb; p=7.69×10^{-4}, n=9,836, Mann-Whitney U-test), which likely explains this phenomenon. Our analyses suggest a possible cell cycle delay and subsequent permanent cell cycle arrest, resulting in cellular senescence in RPB1-K1268R cells in response to DNA damage.

Polr2a$^{K1268R/K1268R}$ / *Xpa*$^{-/-}$ double-mutant mice display short life span and a premature ageing phenotype

Having established a TC-NER-compromised cellular phenotype in RPB1-K1268R cells, we decided to examine the consequences of deficient RNAPIIo ubiquitination in a whole organism. We generated gene-edited mice with the RPB1-K1268R mutation. The RPB1-K1268R mutation was introduced into the *Polr2a* gene in C57BL/6 mouse by CRISPR/Cas9 (see **STAR Methods**). *Polr2a*$^{K1268R/K1268R\ (KR/KR)}$ homozygous knock-in mice were generated after backcrosses of heterozygous founder mice and their inbreeding, which were born with expected Mendelian inheritance ratios. Neither the *Polr2a*$^{KR/KR}$ homozygous, nor the *Polr2a*$^{WT/\ KR}$ heterozygous mice displayed any remarkable abnormalities during the first year of farming. The mice are fertile and their weight and appearance are normal (**Figure S7A**, **Table S4**).

Indeed, in contrast to human CS individuals, TC-NER-deficient *Csa*$^{-/-}$ or *Csb*$^{-/-}$ mice do not show an obvious phenotype (van der Horst et al., 1997). A similar situation is observed in Fanconi anemia (FA) repair pathway (FANC)-deficient mice, which do not develop FA (Chen et al., 1996; Parmar et al., 2009). However, strong

features of FA can be revealed by the genetic deletion of the aldehyde-catabolising enzyme *Aldh2* in FANC-deficient mice (Langevin et al., 2011). Strikingly, clear CS-like features were reported in *Csb*$^{-/-}$ / *Xpa*$^{-/-}$ or *Csb*$^{-/-}$ / *Xpc*$^{-/-}$ double mutant mice (Laposa et al., 2007; van der Pluijm et al., 2007), suggesting that increasing the DNA damage load due to GG-NER deficiency in *Csb*$^{-/-}$ or *Csa*$^{-/-}$ mutants now reveals a CS-like phenotype in mice.

In view of the above, we decided to generate *Polr2a*$^{KR/KR}$ / *Xpa*$^{-/-}$ double mutant (DM) mice to increase the likelihood of RNAPIIo colliding into DNA lesions during transcription and to reveal a potential CS-like phenotype. The DM mice displayed a remarkable growth retardation, low bodyweight, and prominent dwarfism (**Figure 7A**), although all the mice were born with expected Mendelian inheritance ratios. Littermates of these mice with other genotypes did not show any growth or neurological abnormalities (**Figures 7A**, **S7B**; **Tables S5**, **S6**), similar to what was previously reported for *Xpa*$^{-/-}$ mice (Nakane et al., 1995). After 3 months, the DM mice gradually lost their bodyweights, which eventually resulted in death at the age of 5-6 months (**Figure 7A**; **Table S6**). Although daily observations confirmed the normal intake of food and water by the DM animals, their life span and condition did not improve. At 4-5 months of age, skeletal abnormalities, such as kyphosis and abnormal gait due to hindlimb dystonia were prominent in the DM mice, some of which also displayed depigmentation as well as cataracts, similar to human CS individuals (Calmels et al., 2018; Laugel, 2013) (**Figures 7B**, **7C**; **Table S6**).

Loss of motor neurons in *Polr2a*$^{K1268R/K1268R}$ / *Xpa*$^{-/-}$ double mutant mice

The appearance of gait abnormalities and clamping hind limbs became evident after weaning in all DM animals, suggesting potential abnormalities in the central or peripheral nervous system. No obvious morphological abnormalities were apparent in the cerebrum and cerebellum of 4-6 months old DM mice, except their small size in proportion to their body size. Interestingly, however, significant activation of astrocytes was observed in DM mice, implying the possibility of neuronal damage in the cerebral cortex (**Figure 7D**).

The gait abnormalities and dystonia in the DM mice could also be explained by motor neuron-specific abnormalities. To monitor potential progressive motor neuron loss, we quantified the number of axons in the spinal ventral roots from DM mice, which showed a terminal phenotype (>5 months). We observed a marked increase in the number of degenerating axons in the DM mice (**Figure 7E**), although the overall number of axons displayed a modest decrease compared to control mice (**Figure 7F**). Immunofluorescent stainings of spinal cords from DM mice also detected the loss of motor neurons (green), as well as activation of microglia (red) and astrocytes (white) (**Figure 7G**). These observations demonstrate that motor neuron degeneration in the DM animals is a late-onset progressive event, which is highly reminiscent of the progression in human CS-individuals. The progressive neurodegenerative phenotype of the DM mice underscores the importance of RPB1-K1268 ubiquitination *in vivo*, and suggests that these CS-like ageing related phenotypes are best explained by a deficiency in RNAPIIo processing and prolonged transcription arrests under high-load of endogenous DNA damage rather than a compromised DNA repair activity associated with TC-NER.

Discussion

Although the ubiquitination of RNA polymerase IIo after UV irradiation in human cells has been known to occur for a considerable time (Bregman et al., 1996), the precise mechanisms and functions underlying this modification have remained unknown. Here we report that a single DNA damage-induced ubiquitination site at RPB1-K1268 regulates both TC-NER and processing of DNA damage-stalled RNAPIIo on chromatin.

RNA polymerase IIo ubiquitination: difference in human versus budding yeast

DNA damage-induced ubiquitination of RNAPIIo is highly conserved from yeast to man. Elegant studies in the yeast *S. cerevisiae* have demonstrated that the ubiquitination of RNAPIIo by the Rsp5 and Def1 ubiquitin ligases is not required for TC-NER, but rather acts as a last resort pathway to remove and degrade RNAPIIo from DNA damage sites (Lommel et al., 2000; Somesh et al., 2005; Somesh et al., 2007; Woudstra et al., 2002). Conversely, we show here that RPB1-K1268 ubiquitination in human cells does directly contribute to TC-NER (**Figure 3F**). While the RPB1-K1268 site and its surrounding amino acid residues are highly conserved in animals and plants, this region is less conserved in *S. cerevisiae* (**Figure S1C**), suggesting that the primary purpose of RNAPIIo ubiquitination between humans and budding yeast is different. In contrast, the RPB1-K1268 site is fairly conserved (*Rpb1*-K1252) in the fission yeast *S. pombe*, which in many ways shows more complex genomic features also found in vertebrate genomes. Interestingly, an *rpb1*-K1252R mutant in *S. pombe* showed increased sensitivity to the UV mimetic 4-NQO in an NER-deficient Δ*rhp14* (human *XPA* homologue) background (**Figure S7C**). This is reminiscent of our *Polr2a*^{K1286R} knock-in mice, which displays a CS-like phenotype in an NER-deficient *Xpa*$^{-/-}$ background. These DNA repair-independent phenomena found in *S.pombe* and mice strongly suggest an evolutionarily conserved molecular mechanism, which underlies the resolution of transcription-damage collision by RNAPIIo ubiquitination at RPB1-K1268 (-K1252 in *S.pombe*) under a high-load of DNA damage.

Players in RNA polymerase IIo ubiquitination in human

The precise mechanisms involved in human RNAPIIo ubiquitination have been multitude and controversial. While earlier studies revealed that RNAPIIo ubiquitination is defective in cells deficient in CSA or CSB (Bregman et al., 1996; Ratner et al., 1998), more recent work by us (Nakazawa et al., 2012) and our current study also implicated UVSSA in this process, perhaps due to its association with deubiquitylase USP7 and the CSB/CSA complex (Fei and Chen, 2012; Nakazawa et al., 2012; Schwertman et al., 2012; Zhang et al., 2012). Additionally, BRCA1/BARD1 (Kleiman et al., 2005; Starita et al., 2005), Elongin-Cullin complexes (Yasukawa et al., 2008), and the HECT E3 ligase NEDD4 (Anindya et al., 2007) have all been implicated in the UV-induced ubiquitination of human RNAPIIo.

Our findings reveal the near-complete loss of ubiquitination in RPB1-K1268R cells, suggesting that this lysine residue represents the main UV-induced ubiquitination site in RNAPIIo. The accompanying paper by Svejstrup *et al.* also underscores the importance of this RPB1-K1268 ubiquitination for a proper transcription shutdown and recovery in response to UV irradiation. Notably, we observed severely reduced ubiquitination in Δ*CSA* cells, as well as complete loss of this modification after

treatment with MLN4924, which suppresses NEDD8 conjugation to cullin-ring type E3-ligases (CRLs) causing their inactivation. These findings suggest that the $CRL4^{CSA}$ E3 ubiquitin ligase complex is a strong candidate to contributes to RPB1-K1268 ubiquitination.

RPB1-K1268 ubiquitination is involved in TC-NER

The data presented in this study demonstrates that RPB1-K1268 ubiquitination is important for TC-NER. Firstly, we show that RPB1-K1268R HeLa cells are very sensitive to UV irradiation and show an impaired recovery of RNA synthesis after UV. Secondly, strand-specific ChIP-seq analysis revealed that RPB1-K1268R cells showed significantly delayed removal of UV-induced DNA lesions from the transcribed strand of active genes. Thirdly, molecular analysis revealed that the recruitment of the core-TFIIH-complex to DNA damage-stalled RNAPIIo was significantly reduced in RPB1-K1268R cells, explaining the cellular TC-NER-compromised phenotype of these cells. This raises the question how RPB1-K1268 ubiquitination positions the TFIIH-complex during TC-NER?

Our data support a model in which the association of CSB/CSA with DNA damage-stalled RNAPIIo is not affected by RPB1-K1268 ubiquitination. In fact, the CSB/CSA complex facilitates RPB1-K1268 ubiquitination upon its association with RNAPIIo, possibly together with other CRL ubiquitin ligases. The recruitment of UVSSA to RNAPIIo is fully dependent on CSB/CSA. Strikingly, the RPB1-UVSSA interaction is enhanced by RPB1-K1268 ubiquitination likely through the ubiquitin-binding VHS domain in UVSSA, which is most striking for mono-ubiquitinated UVSSA at K414. Although UVSSA initially associates with the TFIIH complex through interactions with the p62 subunit, UVSSA is eventually ubiquitinated at K414 to stimulate the displacement of p62 from UVSSA, possible in concert with other NER proteins. These parallel ubiquitination events of RPB1-K1268 and UVSSA-K414 facilitate the transfer of TFIIH to the DNA damage-stalled RNAPIIo (**Figure 3F**).

RPB1-K1268 ubiquitination has a role in damage-stalled RNAPIIo processing: implications for neurodegeneration

Our molecular analysis revealed that cells deficient in either CSB, CSA, UVSSA, or RPB1-K1268 ubiquitination show a pronounced TC-NER deficiency. Strikingly, however, only defects in the *CSA* or *CSB* genes in humans cause the neurodegenerative disorder Cockayne syndrome (CS), which is characterised by dysmyelination, progressive loss of neurons, severe developmental abnormalities and premature ageing. Conversely, defects in *UVSSA* cause the mild UV-sensitive syndrome ($UV^{S}S$) without devastating features seen in CS, implying that CS is not caused by compromised TC-NER (Nakazawa et al., 2012).

Our current findings shed light on the molecular pathogenesis of CS by revealing that *Polr2a*^{K1286R} mice deficient in the DNA damage-induced ubiquitination of RNAPIIo show pronounced dwarfism, growth retardation, neurodegeneration and short life-span reminiscent of CS. This phenotype only became prominent in DNA repair-compromised *Xpa*$^{-/-}$ background, which lack both GG-NER and TC-NER activity, but display no obvious characteristics including neurological abnormalities, although *Xpa*$^{-/-}$ mice are skin-cancer predisposed after UV irradiation (Nakane et al., 1995). This is in line with the absence of CS-like neurodegeneration in human XP-A

individuals (Brooks, 2008). Importantly, our findings strongly argue that CS-like features are not caused by defective TC-NER. Indeed, neurodegeneration in *Csb*$^{-/-}$ mice was also only observed in an NER-compromised background, such as *Xpa*$^{-/-}$ or *Xpc*$^{-/-}$ mice (Laposa et al., 2007; van der Pluijm et al., 2007), suggesting that this phenotype, in mice, is only unmasked by an excess of unrepaired endogenous DNA lesions ordinarily dealt with by NER. We have noted previously that *CSA* or *CSB*-deficient primary fibroblasts fail to degrade RNAPIIo after UV irradiation, while *UVSSA*-deficient cells showed swift degradation (Nakazawa et al., 2012). This has led to a hypothesis in which a deficiency in RNAPIIo processing and prolonged transcription arrests in response to DNA damage rather than a compromised TC-NER activity underlies the CS-like neurodegenerative phenotype (Nakazawa et al., 2012). The CS-like phenotype of the *Polr2a*^{K1286R} mice fully supports this model. In addition to the intrinsic TC-NER-deficiency, a failure to ubiquitinate RPB1-K1268 leads to a non-displaceable RNAPIIo molecule, which blocks accessibility of the DNA lesions to alternative repair pathways, like GG-NER, and causes prolonged transcription arrests. Indeed, aldehydes and cyclopurines are likely endogenous DNA lesions in the brain that block RNAPIIo progression, and may strongly contribute to the CS phenotype in case RNAPIIo processing is compromised. This model provides an explanation for the different clinical features associated with TC-NER-deficiency disorders. Similarly, defects in processing of RNAPII at various types of DNA damage may contribute to develop neurodegenerative phenotype shared among genome instability disorders.

Acknowledgments

This paper is dedicated to the memory of a wonderful lady, Amy Garton-Hughes, who made a huge difference in the lives of Cockayne syndrome children. We are grateful to Drs. Alan Lehman and Chikahide Masutani for their helpful comments and discussions on the manuscript. We are grateful to Dr. Masato Kanemaki for his advice on the CRIPSR/Cas9-based gene targeting experiments. Bioinformatics data processing was partially performed using the super-computing resource provided by Human Genome Center, the Institute of Medical Science, the University of Tokyo. This work was supported by Special Coordination Funds for Rare and Intractable Diseases from Japan Agency for Medical Research and Development (AMED) (JP19ek0109281, JP19ek0109229, JP19ek0109301), Grants in aid for Scientific Research KAKENHI (JP15H02654, JP17H00783) from Japan Society for the Promotion of Science, a Science Research Grant from Uehara Memorial foundation, a Grant from Daiko Foundation, and a medical research grant from Takeda Science Foundation to T.O.; KAKENHI (JP17H01877), and a medical research grant from Takeda Science Foundation to Y.N.; TBRF Postdoctoral Fellowship for Asian Researchers in Japan from The Tokyo Biochemical Research Foundation (TBRF) to C.G. and T.O.; an LUMC research fellowship and an NWO-VIDI grant (016.161.320) to M.S.L.

Author Contributions

T.O. designed the study and experiments. Y.N., Y.O., D.V.H., C.G., Y.D., M.I., Y.He., M.S., K.K., N.J., S.H., M.S.L, and T.O. performed molecular and cell biological experiments. Y.Hara., and T.O. performed bioinformatics analyses. Y.O., O.K., C.G., Y.He., M.S., Y.K., Y.M., M.T., A.S., T.M., K.Y., and T.O. performed animal studies. N.M and S.N. contributed to materials. N.M., T.S., A.M., K.O., S.N., T.M., K.Y., M.S.L., and T.O. coordinated the study. M.S.L. and T.O. wrote the manuscript. Y.Hara., Y.O., O.K., D.V.H., C.G. and Y.D. contributed equally to the study. T.M. and K.Y. contributed equally to the study. All authors commented on the manuscript.

Declaration of Interests

The authors declare no competing interests.

Main Figure Titles and Legends

Figure 1 RPB1 ubiquitination at K1268 regulates TC-NER and UV survival
(**A**) RPB1 ubiquitination sites (black, all lysine residues; green, putative ubiquitination sites; red, K1268).
(**B**) Detection of the unmodified, and ubiquitinated forms (upper bands, IIo-ubi) of RNAPIIo in chromatin fraction using the 3E10 antibody in the wild-type (WT), indicated RPB1-KR mutants, and Δ*CSB* HeLa cells at 1 h after UV.
(**C**) RRS assay in the indicated RPB1-K1268R clones and Δ*CSB* and Δ*UVSSA* HeLa cells. Cells were UV irradiated (closed bars, 5 J/m^2; open bars, without UV), followed by 12 h incubation with 5-EU (Nakazawa et al., 2010). Results for the other RPB1-KR mutants are shown in **Figure S1E**. Bars represent means and standard deviations (SD) of quintuple wells.
(**D**) Clonogenic UV survival was measured on the RPB1-KR mutant HeLa cells. WT (black); RPB1-K1268R (blue); Δ*CSB* and Δ*UVSSA* (green); KR mutants (sky blue). Error bars represent S.D. of triplicate experiments.

Figure 2 RPB1 ubiquitination at K1268 is dependent on CRL E3 ligase activity
(**A**) RNAPIIo ubiquitination was detected in 48BR fibroblasts treated with or without neddylation inhibitor (MLN4924) for 1 h, followed by UV and further 1 h incubation. Lack of Cullin neddylation was confirmed (Cul4A).
(**B**) Normal (48BR), GG-NER-deficient (XP-C), TC-NER-deficient (CS-B), and full NER-deficient (XP-A) cells were treated with MLN4924 (+, 10μM; -, DMSO) for 1 h, followed by RRS measurements after UV (13 J/m^2). Bars represent means (SD) of quintuple wells.
(**C**) Affinity purification of Strep-Ubiquitin (WT or the indicated KR mutants) from WT HEK293 cells at 1 h after UV. Both ubiquitinated- and unmodified-RPB1-IIo were detected (RNAPII-Ser2). Ubiquitin chain termination products were detected in cells expressing Ubiquitin-K48R, or -K63R mutants. Total ubiquitinated proteins (Myc). WCE, whole cell lysate.
(**D**) Affinity purification of GFP-RPB1 (WT) from either WT or Δ*CSA* HEK293 cells, or GFP-RPB1 K1268R from WT cells at 1 h after UV.

Figure 3 TFIIH recruitment is dependent on the ubiquitination of RPB1-K1268 and UVSSA-K414
(**A**) Co-IP with RNAPII-Ser2 antibody (Ab5095) at 1 h after with- or without-UV from the chromatin fraction of WT or RPB1-K1268R (K1268R) HeLa cells. The input is 1.5% of the chromatin fraction. RNAPII was detected with 3E10 (Ser2) and 3E8 (Ser5) antibodies. Asterisks represent non-specific products. Results for the other RPB1-KR mutants are shown in **Figure S3B**.
(**B**) Co-IP as in A from WT, Δ*UVSSA,* or *UVSSA* knockin with a K414 deletion (ΔK414) HeLa cells at 1 h after UV irradiation. No UVSSA ubiquitination was detected in the ΔK414 cells.
(**C**) Co-IP as in A from WT or RPB1-K1268R HeLa cells at 1 h after UV irradiation. Note that the amount of ubiquitinated UVSSA interacting with RPB1-IIo was reduced in RPB1-K1268R mutant.

(D) Co-IP as in A from the indicated HeLa cells (WT, RPB1-K1286R, Δ*CSB*) after UV, followed by incubation for the indicated time periods. FK2 antibody detects ubiquitinated RPB1-IIo in WT cells.
(**E**) Co-IP as in A from the indicated HeLa cells (WT, Δ*UVSSA*, and Δ*UVSSA* with ectopic expression of the indicated V5-tagged *UVSSA* variants) at 1 h after UV irradiation. UVSSA K414 ubiquitination is critical for the TFIIH recruitment.
(**F**) Working model for the recruitment of TFIIH. **1**: RNAPIIo stalls at DNA damage. **2**: The CRL^{CSA} complex, possibly in concert with another E3-ligases ubiquitinates RPB1-K1268; UVSSA is also recruited by CSB/CSA. **3**: VHS domain supports the UVSSA interaction with ubiquitinated RPB1-IIo; UVSSA recruits TFIIH-p62 via PH-domain binding sequence (PHB). **4**: Mono-ubiquitination of UVSSA-K414 facilitates transfer of TFIIH to RPB1-IIo.

Figure 4 Strand-specific ChIP-seq enables precise spaciotemporal mapping of RPB1-IIo molecules stalled at DNA damage sites
(**A**) Schematic representation of RNAPII ChIP-seq, which was performed with anti-RPB1 phopho-CTD specific antibodies. After decrosslinking, DNA lesions remain in the template strand. Strand-specific NGS libraries were prepared for the Illumina platform (see also **E**).
(**B**, **C**) Distributions of chromatin-bound RNAPII (RPB1-Ser2, 3E10; -Ser5, 3E8) within gene bodies and flanking regions (**B**) 3 h or (**C**) 12 h after 7J/m^2 UV irradiation in either WT or RPB1-K1268R HeLa cells. Note that no obvious difference in RNAPII distribution was observed between WT and RPB1-K1268R mutant without UV (gray lines). Without UV data are identical in (**B**) and (**C**). Additional plots for other time points, for pan-RPB1, and for TC-NER-deficient cells are shown in **Figures S4A**, **S4B**.
(**D**) RNAPIIo distribution changes in individual genes after UV irradiation. RPB1-Ser2 ChIP-seq read coverages (RPM: reads per million mapped reads) in representative genes in (**B**) and (**C**) are shown.
(**E**) Schematic representation of the strand-specific ChIP approach (RPB1-Ser2, 3E10). Calculation of the strand-specificity index (SSI) is detailed in **STAR Methods**. Left panel: The asymmetric adapters for Illumina libraries allow preferential amplification of DNA strands without damage, resulting in a retention of directional information (see also **A**). Right-upper panel: Strand-biased ChIP-seq reads associated with the gene orientation are shown for representative genes. Without UV, RPM of forwardly mapped reads and reversely mapped reads are similar and no strand specificity is detected (absolute SSI value, |SSI|=0). At 3 h after UV, |SSI| increases due to the presence of DNA lesions in the transcribed strand. Right-bottom panel: Scatter plots of SSI against RPM within gene bodies in individual 'active genes' (9,836 genes, see definition in **Figure S4C**). Unimodal SSI distribution is observed in a representative sample without DNA damage, while bimodal distribution appears 3 h after UV irradiation. Plots reused in (**G**). Number of mapped reads within +301bp to +2 kb was counted for RPM in the plots.
(**F**) ChIPed DNA (RPB1-Ser2, Ab5095) from UV-irradiated (3 h after 7 J/m^2) WT HeLa cells was treated with DNA damage repair enzyme mix for 20 min, or 2 h prior to library preparation. Note that the bimodal distribution disappeared (purple).
(**G**) SSI scatter plots of active genes in WT (red) or RPB1-K1268R (blue) HeLa cells after UV irradiation (7 J/m^2) based on strand-specific ChIP-seq (RPB1-Ser2, 3E10). All

the plots employed active genes. Plots reused in **Figure S4E**. *P*-values were calculated with the Wilcoxon signed rank test (n=9,836), and were corrected by the Benjamini-Hochberg method. Scatter plots of the samples from other time points, as well as TC-NER-deficient cells are shown in **Figure S4E**.

Figure 5 Slow DNA repair kinetics of transcribed strands in RPB1-K1268R mutant

(**A**) Strand-specific ChIP-seq (RPB1-Ser2, 3E10) read distribution in a representative gene (*MCM3*) showing slow repair kinetics in RPB1-K1268R (blue) compared to WT (red) cells after UV (7 J/m^2). |SSI| calculated for *MCM3* gene body and PTPS regions are indicated.

(**B**) Time course in the indicated HeLa cells of the recovery index (RI), representing the progression of DNA lesion removal from transcribed strands in the entire active genes. The RI is derived from a mixture of Gaussians that correspond to the unrepaired gene fractions (i.e. |SSI|<>0) in the gene-by-gene SSI distribution of RPB1-Ser2 ChIPseq (3E10) (see also **Figure S5A**). The RI was calculated from duplicate time-course experiments shown in **Figures 4G**, **S4E**, and the curves were fitted to gamma functions.

(**C**) Time course of median |SSI| across relative position in gene bodies in whole active genes. In this analysis, 'central genic region' (>20 kb active genes) were used in order to exclude the effects of mapped reads nearby TSS and TES. This selection did not affect the RI kinetics (See **Figure S5B**). No positional preference of damage removal from gene bodies was detected. SSI data same as in (**B**). Results of early time points after UV irradiation are shown in **Figure S5D** (3 h data replotted).

(**D**) Time-course of RNAPIIo accumulation at T-T dimer sites. Mapped reads enrichments in the coding strand (ApA, A<>A) are shown (central genic region of >20 kb active genes). Colored humps represent delayed T-T dimer removal in RPB1-K1268R mutant and TC-NER-deficient cells. ChIP-seq data same as in (**B**). Results of late time points after UV irradiation is shown in **Figure S5F** (3 h data replotted). RPGC represents 1x depth of coverage (reads per genome coverage).

(**E**) Asymmetric distribution of the mapped reads in the coding strand immediately adjacent to A<>A dimer sites (h_a) and in the 5' lesion-proximal region (h_b) shown for the central genic region of >20 kb active genes in chr 1 (left panel). Note that the base line at the 5' lesion-proximal region (h_b) is higher than that at the 3' side, indicating stalling of RPB1-IIo at the DNA lesion causing 'queueing' of multiple RNAPIIo. The queue formation kinetics is identical in all cell types, while the resolution is fastest in WT (dashed lines). Data in (**D**, **Figure S5F**) are analysed.

Figure 6 Gene-by-gene repair profiles in RPB1-K1268R mutant

(**A**) Strong gene-by-gene correlation of SSI (RPB1-Ser2, 3E10) between biological replicates in WT and RPB1-K1268R mutant HeLa cells. The genes presenting significantly high SSI are shown as red dots (Spearman's correlation coefficient was calculated for each pair). Those correlations between replicates of TC-NER-deficient cells are shown in **Figure S6A**.

(**B**) Venn diagram indicates the numbers of genes displaying significantly high SSI at 12 h after UV irradiation (representing the numbers of red dots in (**A**, **S6A**)). About 80 % of unrepaired genes are overlapping between RPB1-K1268R (KR) and TC-NER-deficient (ΔTCR) cells.

(**C**, **D**, **E**) Violin plots displaying distributions of gene lengths (**C**), GC contents (**D**), and read-density in gene bodies (**E**) for individual genes in the gene-sets determined in (**B**). *P*-values were calculated with Mann-Whitney *U*-test, and were corrected by the Benjamini-Hochberg method.
(**F**) Strand-specific read distributions in representative 'unrepaired genes' in RPB1-K1268R cells with profiles shown in (**C**, **D**, **E**).

Figure 7 RPB1-IIo K1268 ubiquitination protects against neurodegeneration in mice

(**A**) Bodyweight distribution and growth curves of mice with the indicated genotypes. Representative control and *Polr2a*$^{K1268R/K1268R\ (KR/KR)}$ / *Xpa*$^{-/-}$ (DM) mice are shown at 144 d (males left, females right). Loss of bodyweight observed only in DM mice from 3 month after birth. Growth curves of mice with the WT *Xpa*$^{+/+}$ genotypes and the heterozygous *Xpa*$^{+/-}$ genotypes are shown in **Figures S7A**, **S7B**, respectively. See also **Tables S4-6**. *Polr2a*$^{WT/WT}$ / *Xpa*$^{-/-}$ ♂ (*n*=9); *Polr2a*$^{WT/KR}$ / *Xpa*$^{-/-}$ ♂ (*n*=22); *Polr2a*$^{KR/KR}$ / *Xpa*$^{-/-}$ ♂ (*n*=5); *Polr2a*$^{WT/WT}$ / *Xpa*$^{-/-}$ ♀ (*n*=12); *Polr2a*$^{WT/KR}$ / *Xpa*$^{-/-}$ ♀ (*n*=18); *Polr2a*$^{KR/KR}$ / *Xpa*$^{-/-}$ ♀ (*n*=7).
(**B**) Representative premature aging phenotypes observed in DM mice. Kyphosis (1), gait abnormalities (2), and slimming (3) in a DM mouse (139 d). Hind limb dystonia (clamping) (4) in a DM mouse (144 d), and a normal (5) *Polr2a*$^{WT/KR}$ / *Xpa*$^{-/-}$ littermate (144 d). Depigmentation (6) in a DM mouse (139 d). Cataract (7; 8, magnified view) in a DM mouse (153 d).
(**C**) Computed tomography images detected a severe kyphosis in a DM mouse (male, 180 d). A normal littermate control is shown (*Polr2a*$^{WT/WT}$ / *Xpa*$^{+/-}$ 180 d).
(**D**) Activation of astrocytes in the cerebral cortex was observed in DM mice (153 d) at an end stage compared to normal control (*Polr2a*$^{WT/\ KR}$ / *Xpa*$^{+/-}$, 153 d) by staining for GFAP (red).
(**E**) Representative images of toluidine blue-stained lumbar 5th ventral roots from a WT (C57BL/6), a control (*Polr2a*$^{WT/\ KR}$ / *Xpa*$^{-/-}$, 181 d), and a DM (163 d) mouse showing terminal phenotype. Degeneration of axons as well as decrease in the numbers of intact axons were observed.
(**F**) The axonal degeneration was observed in DM mice showing terminal phenotype. Average numbers of lumbar 5th motor axons are plotted (WT, C67BL/6, *n*=3; control, *Polr2a*$^{WT/\ KR}$ / *Xpa*$^{-/-}$, *n*=3; DM, *n*=3). Data presented as means (SD). *P*-values were calculated with one-way ANOVA, followed by Tukey-Kramer *post hoc* tests.
(**G**) Loss of motor neurons as well as increase in the numbers of microglia and reactive astrocytes was observed in lumbar spinal cords (boxed regions) of a DM mouse at an end stage (166 d), compared to control *Polr2a*$^{WT/\ KR}$ / *Xpa*$^{-/-}$ (166 d) mice. Representative immunofluorescent images of lumbar spinal cord sections are shown stained for ChAT (green), Iba1 (red), GFAP (white).

Supplemental Figure Titles and Legends

Figure S1 RNAPII is ubiquitinted at RPB1-K1268, Related to Figure 1

(**A**) Immunostainings of UV-induced RPB1-IIo upper bands overlap with staining for conjugated ubiquitin. The pictures are cropped from **Figure 3D** (WT, IP-RPB1-Ser2; RNAPII (Ser2), Ubiquitin; UV-, 1 h) and superimposed to indicate overlapping bands. Wild type HeLa cells were UV irradiated (20 J/m^2), followed by 1h incubation. RPB1-IIo (red) and polyubiquitinated proteins (green) were respectively detected as described in **Figure 3D**.

(**B**) UV induced RPB1-IIo upper bands are consist of ubiquitin chains. Cells stably expressing GFP-tagged wild type RPB1 (GFP-RPB1) were UV irradiated (20 J/m^2), followed by 1 h incubation. Affinity purification was performed with GFP-Trap conjugated beads under an SDS-denaturing condition. Partially purified GFP-RPB1 proteins were incubated with USP2 ubiquitin endoprotease. GFP-RPB1-IIo and cleaved ubiquitin were detected as described in **Figure 2D**.

(**C**) RPB1-K1268 is evolutionarily conserved in broad taxa. Multiple alignment was performed using MAFFT program. Amino acid residues correspond to human RPB1-K1268 is shown in green.

(**D**) RPB1-K1268 is surface-exposed near to where the downstream DNA enters RNAPII. RPB1 structures were reconstructed by CCP4MG software (v. 2.10.10) using the PDB data entry, 5IY9 (He et al., 2016). The K1268 residue is shown in red, while other putative ubiquitynated lysine residues are shown in blue.

(**E**) Recovery of RNA synthesis (RRS) after UV irradiation in RPB1-KR mutant HeLa cells shown in **Figure 1B**. WT, wild-type , Δ*CSB* and Δ*UVSSA* for controls. Cells were UV irradiated (closed bars, 5 J/m^2 UV; open bars, without UV), followed by 12h incubation for RNA synthesis recovery. RRS levels measured as in **Figure 1C**. Bars represent means (SD) of quadruple wells.

(**F**) Normal nascent transcription levels in RPB1-K1268R mutant. Ethynyluridine (EU)-incorporation for non-UV irradiated samples were shown. Fluorescent data obtained from **S1E**. Bars represent means (SD) of quadruple wells.

Figure S2 RPB1-K1268 ubiquitination is dependent on CSA, Related to Figure 2

UV inducible ubiquitin chain formation on RPB1-K1268 residue. Strep-tagged Ubiquitin was transiently expressed in wild type, Δ*CSA*, and RPB1-K1268R HeLa cells. Cells were 20 J/m^2 UV irradiated, followed by 1h incubation. Affinity purification of ubiquitinated proteins was performed with Strep-Tactin conjugated beads under an SDS-denaturing condition. RPB1-Ser2 was detected as in **Figure 1B**. Discrete upper bands were detected in the UV irradiated wild type cells and significant reduction of the bands was observed in the RPB1-K1268R and Δ*CSA* cells. RAD21, loading control (D213). Asterisk represents nonspecific products.

Figure S3 UVSSA ubiquitination regulates TFIIH recruitment, Related to Figure 3

(**A**) CSA, CSB, and UVSSA are all required for the TFIIH recruitment to damage stalled RPB1 after UV irradiation. Wild-type (WT), Δ*CSA*, Δ*CSB*, and Δ*UVSSA* HeLa cells were UV irradiated (+, 20 J/m^2 UV , without UV), followed by 1h incubation. Co-immunoprecipitation of RPB1-Ser2 (Ab5095) and detection of interacting factors are as in **Figure 3A**.

(**B**) Normal TFIIH recruitment in RPB1-KR mutants except RPB1-K1268R. Wild-type (WT) and RPB1-KR mutant HeLa cells used in **Figure 1B** were UV irradiated (+, 20 J/m^2 UV , without UV), followed by 1h incubation. Co-immunoprecipitation of RPB1-Ser2 (Ab5095) and detection of interacting factors are as in **Figure 3A**.
(**C**) Normal TFIIH recruitment during transcription initiation in RPB1-K1268R mutant. Wild-type (WT) and RPB1-K1268R mutant HeLa cells were UV irradiated (+, 20 J/m^2 UV; -, without UV), followed by 1 h incubation. Co-immunoprecipitation of RPB1-Ser2 (Ab5095) and RPB1-Sre5 (3E8), as well as detection of interacting factors are as in **Figure 3A**. Recruitment of p89 was not abrogated in RPB1-K1268R mutant in RPB1-Ser5 immunoprecipitants.
(**D**) UVSSA-K414R mutant maintains TFIIH interaction. Δ*UVSSA* HeLa cells expressing the V5-tagged wild-type (WT) UVSSA and its PH-domain binding sequence (PDB) mutants (UVSSA-F408A, -V411A) as well as K414 mono-ubiquitination site mutant (UVSSA-K414R) were UV irradiated (+, 20 J/m^2 UV , without UV), followed by 1h incubation. Co-immunoprecipitation of V5-tagged UVSSA as well as detection of interacting factors are as in **Figure 3A** except using an anti-V5 antibody (PM003).
(**E**) UVSSA-PH-binding domain sequence (PDB) and mono-ubiquitination site are essential for TC-NER activity. HeLa cells used in **Figures 3B**, **3E** were UV irradiated (6 J/m^2), followed by RRS measurements as described in **Figure 1C**. Bars represent means (SD) of triplicate wells.

Figure S4 Strand-specific ChIP-seq for TC-NER mutants, Related to Figure 4
(**A**) Distributions of chromatin-binding RNAPII molecules within gene bodies and flanking regions at designated time points after UV irradiation. ChIP-seq and analyses performed as in **Figures 4B**, **4C**. ChIP-seq read coverage represents RNAPII distribution for wild-type (dashed lines, identical in the figures), RPB1-K1268R (K1268R), Δ*CSB*, Δ*CSA*, and Δ*UVSSA* (solid lines) HeLa cells (without UV, gray lines; 7 J/m^2 UV, coloured lines for RPB1-Ser2, green; -Ser5, orange; and for total-RPB1 molecules, red coloured lines). The Data for wild-type and RPB1-K1268R (without UV, 3 h, 12 h) are identical to which shown in **Figures 4B**, **4C**. Arrows indicate the accumulation of RNAPII-Ser2 reads after UV near TSS in TC-NER-deficient cells.
(**B**) Distributions of chromatin-binding RPB1-Ser2 (3E10) within gene bodies and flanking regions at designated time points after UV irradiation (7 J/m^2). Early time points data for the cells in **S4A** are shown. The Data for without UV are identical to which shown in **Figure S4A**.
(**C**) Determination of the 'active genes'. Pan-RPB1 ChIP-seq data from non-UV irradiated wild type HeLa cells were used to determine the active genes as those exhibiting totally mapped reads nearby TSS (-100 to + 300 bp) > 0.6 reads per million mapped reads. Distributions of chromatin-binding RNAPII molecules (pan-RPB1) within gene bodies and flanking regions in active (green) and inactive (orange) genes are shown.
(**D**) Relationship of the mapped read depths of whole individual genes between biological replicates (RPB1-Ser2, 3E10, 7 J/m^2). Read depth was denoted by reads per kilobase of gene body per million mapped reads (RPKM). Spearman's correlation coefficient was calculated for each pair (n=17,786).
(**E**) Scatter plots of SSI (RPB1-Ser2, 3E10, 7 J/m^2) against the density of mapped reads within individual 'active genes' (see **Figure S4C**) for wild-type (WT), RPB1-K1268R

(K1268R), and TC-NER-deficient (Δ*UVSSA*, Δ*CSB*, Δ*CSA*) cells at designated time points. The plots of wild-type and RPB1-K1268R (without UV, 3 h, and 12 h) are identical to which shown in **Figure 4G**.

Figure S5 DNA repair kinetics of transcribed strands, Related to Figure 5

(**A**) Definition of Recovery index. We assume that a distribution frequency of the gene-by-gene strand specificity index (SSI) follows the mixed Gaussian distribution, comprising three normal distributions, where the two peripheral normal distributions are symmetric with respect to x=0. The parameters were inferred with a maximum-likelihood framework using the fitdistr function implemented in the MASS package in R. A representative histogram obtained from RPB1-Ser2 ChIP from wild-type HeLa cells 3 h after 7 J/m^2 UV irradiation in **Figure 4G**.

(**B**) Time course of recovery index (RI) calculated for the 'central genic region' (from 5 kb downstream of TSS to 5 kb upstream of TES) of >20 kb active genes. RI curves (calculated from the same data in **Figure 5B**) are nearly identical to those calculated for the entire gene. See **Figure 5B** for details.

(**C**) Time course of the denominator (dashed lines, *fwd* + *rev*) and the absolute value of the numerator (sold lines, |*fwd* - *rev*|) of the gene-by-gene SSI (RPB1-Ser2, 3E10, 7 J/m^2). These values were calculated as RPKM (reads per kilo base pairs per million) for the 'central genic region' of >20 kb active genes. Medians of the individual values were plotted at each time point.

(**D**) Time course of median SSI (RPB1-Ser2) across relative position in gene bodies in whole active genes (central genic region of >20 kb active genes) (3 h or earlier time points after 7 J/m^2 UV irradiation). See **Figure 5C** for details (3 h data replotted).

(**E**) Stalled RNAPIIo accumulation at T-T dimer (A<>A in the coding strand) sites in chr 1 (central genic region of >20 kb active genes). The plot indicates abundance of ChIP-seq mapped reads in the coding strands adjacent to A<>A dimers in chr 1, due to the preferential amplification of undamaged strands. The data same as in **Figure S5F** (WT, RPB1-Ser2, 3E10, 3h after 7 J/m^2). RPGC represents 1x depth of coverage (reads per genome coverage).

(**F**) Time course of RPB1-Ser2 accumulation at T-T dimer (A<>A in the coding strand) sites 3 h or later after UV irradiation (central genic region of >20 kb active genes, 3E10, 7 J/m^2). Results of earlier time points were shown in **Figure 5D** (3 h data replotted). RPGC represents 1x depth of coverage (reads per genome coverage).

Figure S6 Gene-by-gene repair profiles in TC-NER mutants, Related to Figure 6

(**A**) Gene-by-gene correlation of SSI between biological replicates in Δ*CSA*, Δ*CSB*, and Δ*UVSSA* HeLa cells. See **Figure 6A** for details.

(**B**) A gene-enrichment analysis identified an accumulation of unrepaired genes in the 'cell cycle' pathway in RPB1-K1268R cells. Genes identified in **Figure 6B** (WT and RPB1-K1268R, 12 h after UV) were analysed using the KEGG (Kyoto Encyclopedia of Genes and Genomes) database. Genes shown in reds are repaired in wild-type but unrepaired in RPB1-K1268R cells. SSIs for wild-type (bottom) and RPB1-K1268R (top) are shown. Genes in green, and yellow respectively represent repaired and unrepaired genes in both wild-type and RPB1-K1268R.

Figure S7 Phenotypes of *Polr2a*-K1268R and *rpb1*-K1252R, Related to Figure 7

(**A**) Growth curves of *Polr2a*$^{K1268R/K1268R}$ single mutant mice. No growth abnormality, in terms of bodyweight and life span, was observed in *Polr2a*$^{K1268R/K1268R}$ (KR/KR) and *Polr2a*$^{WT/K1268R}$ (WT/KR) compared to wild type (WT/WT). Left panel, male; right panel, female. *Polr2a*$^{WT/WT}$ ♂ (*n*=9); *Polr2a*$^{WT/KR}$ ♂ (*n*=6); *Polr2a*$^{KR/KR}$ ♂ (*n*=10); *Polr2a*$^{WT/WT}$ ♀ (*n*=7); *Polr2a*$^{WT/KR}$ ♀ (*n*=17); *Polr2a*$^{KR/KR}$ ♀ (*n*=9).
(**B**) Bodyweight distribution and growth curves of *Polr2a*$^{KR/KR}$ / *Xpa*$^{+/-}$ mice. *Xpa*$^{+/-}$ genotype is insufficient to induce high-load of endogenous DNA damage; *Polr2a*$^{KR/KR}$ / *Xpa*$^{+/-}$ mice did not elicit growth abnormality. WT/WT, *Polr2a*$^{WT/WT}$ / *Xpa*$^{+/-}$ (♂, *n*=5; ♀, *n*=6); WT/KR, *Polr2a*$^{WT/KR}$ / *Xpa*$^{+/-}$ (♂, *n*=13; ♀, *n*=14); KR/KR, *Polr2a*$^{KR/KR}$ / *Xpa*$^{+/-}$ (♂, *n*=13; ♀, *n*=6). Left panel, male; right panel, female.

(**C**) *S.pombe rpb1*-K1252R mutant displays a sensitivity to UV-mimetic 4NQO. Spot test analyses were performed on the *S. pombe* RPB1-K1252R strains with YES plates containing indicated concentrations of 4-Nitroquinoline 1-Oxide (4NQO). WT (*rpb1*$^{+}$) and KR respectively indicate the wild-type and K1252R RPB1 alleles. *rpb1*-K1252R *rhp14*::*NatMX6* double mutant displayed a synergistic effect. NER^{+}, NER-proficient; *rhp14*::*NatMX6*, Δ*XPA* homologue; *rhp26*:: *NatMX6*, Δ*CSB* homologue.

References

Aboussekhra, A., Biggerstaff, M., Shivji, M.K., Vilpo, J.A., Moncollin, V., Podust, V.N., Protic, M., Hubscher, U., Egly, J.M., and Wood, R.D. (1995). Mammalian DNA nucleotide excision repair reconstituted with purified protein components. Cell *80*, 859-868.

Anindya, R., Aygun, O., and Svejstrup, J.Q. (2007). Damage-induced ubiquitylation of human RNA polymerase II by the ubiquitin ligase Nedd4, but not Cockayne syndrome proteins or BRCA1. Mol Cell *28*, 386-397.

Bähler, J., Wu, J.Q., Longtine, M.S., Shah, N.G., McKenzie, A., Steever, A.B., Wach, A., Philippsen, P., and Pringle, J.R. (1998). Heterologous modules for efficient and versatile PCR-based gene targeting in Schizosaccharomyces pombe. Yeast. *14*, 943-951.

Bolger, A.M., Lohse, M., and Usadel, B. (2014). Trimmomatic: a flexible trimmer for Illumina sequence data. Bioinformatics *30*, 2114-2120.

Bregman, D.B., Halaban, R., van Gool, A.J., Henning, K.A., Friedberg, E.C., and Warren, S.L. (1996). UV-induced ubiquitination of RNA polymerase II: a novel modification deficient in Cockayne syndrome cells. Proc Natl Acad Sci U S A *93*, 11586-11590.

Brookes, E., de Santiago, I., Hebenstreit, D., Morris, K.J., Carroll, T., Xie, S.Q., Stock, J.K., Heidemann, M., Eick, D., Nozaki, N.*, et al.* (2012). Polycomb associates genome-wide with a specific RNA polymerase II variant, and regulates metabolic genes in ESCs. Cell stem cell *10*, 157-170.

Brooks, P.J. (2008). The 8,5'-cyclopurine-2'-deoxynucleosides: Candidate neurodegenerative DNA lesions in xeroderma pigmentosum, and unique probes of transcription and nucleotide excision repair. DNA Repair (Amst) *7*, 1168-1179.

Brueckner, F., Hennecke, U., Carell, T., and Cramer, P. (2007). CPD damage recognition by transcribing RNA polymerase II. Science *315*, 859-862.

Calmels, N., Botta, E., Jia, N., Fawcett, H., Nardo, T., Nakazawa, Y., Lanzafame, M., Moriwaki, S., Sugita, K., Kubota, M.*, et al.* (2018). Functional and clinical relevance of novel mutations in a large cohort of patients with Cockayne syndrome. J Med Genet *55*, 329-343.

1 Chen, M., Tomkins, D.J., Auerbach, W., McKerlie, C., Youssoufian, H., Liu, L.,
2 Gan, O., Carreau, M., Auerbach, A., Groves, T.*, et al.* (1996). Inactivation of
3 Fac in mice produces inducible chromosomal instability and reduced fertility
4 reminiscent of Fanconi anaemia. Nat Genet *12*, 448-451.

5 Elia, A.E., Boardman, A.P., Wang, D.C., Huttlin, E.L., Everley, R.A., Dephoure,
6 N., Zhou, C., Koren, I., Gygi, S.P., and Elledge, S.J. (2015). Quantitative
7 Proteomic Atlas of Ubiquitination and Acetylation in the DNA Damage
8 Response. Mol Cell *59*, 867-881.

9 Fedorov A., Beichel R., Kalpathy-Cramer J., Finet J., Fillion-Robin J-C., Pujol
10 S., Bauer C., Jennings D., Fennessy F., Sonka M., Buatti J., Aylward S.R.,
11 Miller J.V., Pieper S., and Kikinis R. (2012). 3D Slicer as an Image Computing
12 Platform for the Quantitative Imaging Network. Magn Reson Imaging *30*, 1323-
13 1341.

14 Fei, J., and Chen, J. (2012). KIAA1530 protein is recruited by Cockayne
15 syndrome complementation group protein A (CSA) to participate in
16 transcription-coupled repair (TCR). J Biol Chem *287*, 35118-35126.

17 Friedberg, E.C., Walker, G.C., Siede, W., Wood, R.D., Schultz, R.A., and
18 Ellenberger, T. (2005). DNA Repair and Mutagenesis, 2 edn (ASM Press).

19 Gregersen, L.H., and Svejstrup, J.Q. (2018). The Cellular Response to
20 Transcription-Blocking DNA Damage. Trends Biochem Sci *43*, 327-341.

21 Haeussler, M., Schönig, K., Eckert, H., Eschstruth, A., Mianné, J., Renaud, J.B.,
22 Schneider-Maunoury, S., Shkumatava, A., Teboul, L., Kent, J., Joly, J.S., and
23 Concordet, J.P. (2016). Evaluation of off-target and on-target scoring algorithms
24 and integration into the guide RNA selection tool CRISPOR. Genome Biol *17*,
25 148.

26 Hanawalt, P.C., and Spivak, G. (2008). Transcription-coupled DNA repair: two
27 decades of progress and surprises. Nat Rev Mol Cell Biol *9*, 958-970.

28 He, Y., Yan, C., Fang, J., Inouye, C., Tjian, R., Ivanov, I., and Nogales, E.
29 (2016). Near-atomic resolution visualization of human transcription promoter
30 opening. Nature *533*, 359-365.

31 Higa, M., Tanaka, K., and Saijo, M. (2018). Inhibition of UVSSA ubiquitination
32 suppresses transcription-coupled nucleotide excision repair deficiency caused
33 by dissociation from USP7. FEBS J *285*, 965-976.

1 Jackson, S.P., and Bartek, J. (2009). The DNA-damage response in human
2 biology and disease. Nature *461*, 1071-1078.

3 Jia, N., Nakazawa, Y., Guo, C., Shimada, M., Sethi, M., Takahashi, Y., Ueda,
4 H., Nagayama, Y., and Ogi, T. (2015). A rapid, comprehensive system for
5 assaying DNA repair activity and cytotoxic effects of DNA-damaging reagents.
6 Nat Protoc *10*, 12-24.

7 Kanehisa, M., and Goto, S. (2000). KEGG: kyoto encyclopedia of genes and
8 genomes. Nucleic Acids Res *28*, 27-30.

9 Kashiyama, K., Nakazawa, Y., Pilz, D.T., Guo, C., Shimada, M., Sasaki, K.,
10 Fawcett, H., Wing, J.F., Lewin, S.O., Carr, L.*, et al.* (2013). Malfunction of
11 nuclease ERCC1-XPF results in diverse clinical manifestations and causes
12 Cockayne syndrome, xeroderma pigmentosum, and Fanconi anemia. Am J
13 Hum Genet *92*, 807-819.

14 Kleiman, F.E., Wu-Baer, F., Fonseca, D., Kaneko, S., Baer, R., and Manley,
15 J.L. (2005). BRCA1/BARD1 inhibition of mRNA 3' processing involves targeted
16 degradation of RNA polymerase II. Genes Dev *19*, 1227-1237.

17 Langevin, F., Crossan, G.P., Rosado, I.V., Arends, M.J., and Patel, K.J. (2011).
18 Fancd2 counteracts the toxic effects of naturally produced aldehydes in mice.
19 Nature *475*, 53-58.

20 Laposa, R.R., Huang, E.J., and Cleaver, J.E. (2007). Increased apoptosis, p53
21 up-regulation, and cerebellar neuronal degeneration in repair-deficient
22 Cockayne syndrome mice. Proc Natl Acad Sci U S A *104*, 1389-1394.

23 Laugel, V. (2013). Cockayne syndrome: the expanding clinical and mutational
24 spectrum. Mech Ageing Dev *134*, 161-170.

25 Li, H., Handsaker, B., Wysoker, A., Fennell, T., Ruan, J., Homer, N., Marth, G.,
26 Abecasis, G., Durbin, R., and Genome Project Data Processing Subgroup
27 (2009). The Sequence Alignment/Map format and SAMtools. Bioinformatics *25*,
28 2078-2079.

29 Li, H. (2013). Aligning sequence reads, clone sequences and assembly contigs
30 with BWA-MEM. https://arxiv.org/abs/1303.3997

31 Limsirichaikul, S., Niimi, A., Fawcett, H., Lehmann, A., Yamashita, S., and Ogi,
32 T. (2009). A rapid non-radioactive technique for measurement of repair

synthesis in primary human fibroblasts by incorporation of ethynyl deoxyuridine (EdU). Nucleic Acids Res *37*, e31.

Ljungman, M., and Zhang, F. (1996). Blockage of RNA polymerase as a possible trigger for u.v. light-induced apoptosis. Oncogene *13*, 823-831.

Lommel, L., Bucheli, M.E., and Sweder, K.S. (2000). Transcription-coupled repair in yeast is independent from ubiquitylation of RNA pol II: implications for Cockayne's syndrome. Proc Natl Acad Sci U S A *97*, 9088-9092.

Marteijn, J.A., Lans, H., Vermeulen, W., and Hoeijmakers, J.H. (2014). Understanding nucleotide excision repair and its roles in cancer and ageing. Nat Rev Mol Cell Biol *15*, 465-481.

Mayer, A., Landry, H.M., and Churchman, L.S. (2017). Pause & go: from the discovery of RNA polymerase pausing to its functional implications. Curr Opin Cell Biol *46*, 72-80.

McKenna, A., Hanna, M., Banks, E., Sivachenko, A., Cibulskis, K., Kernytsky, A., Garimella, K., Altshuler, D., Gabriel, S., Daly, M.*, et al.* (2010). The Genome Analysis Toolkit: a MapReduce framework for analyzing next-generation DNA sequencing data. Genome Res *20*, 1297-1303.

Menoni, H., Wienholz, F., Theil, A.F., Janssens, R.C., Lans, H., Campalans, A., Radicella, JP., Marteijn, J.A., and Vermeulen, W. (2018). The transcription-coupled DNA repair-initiating protein CSB promotes XRCC1 recruitment to oxidative DNA damage. Nucleic Acids Res *46*, 7747-7756.

Moreno, S., Klar, A., and Nurse, P. (1991). Molecular genetic analysis of fission yeast Schizosaccharomyces pombe. Methods Enzymol *194*, 795-823.

Naito, Y., Hino, K., Bono, H., and Ui-Tei, K. (2015). CRISPRdirect: software for designing CRISPR/Cas guide RNA with reduced off-target sites. Bioinformatics, *31*, 1120–1123.

Nakane, H., Takeuchi, S., Yuba, S., Saijo, M., Nakatsu, Y., Murai, H., Nakatsuru, Y., Ishikawa, T., Hirota, S., Kitamura, Y.*, et al.* (1995). High incidence of ultraviolet-B-or chemical-carcinogen-induced skin tumours in mice lacking the xeroderma pigmentosum group A gene. Nature *377*, 165-168.

Nakazawa, Y., Sasaki, K., Mitsutake, N., Matsuse, M., Shimada, M., Nardo, T., Takahashi, Y., Ohyama, K., Ito, K., Mishima, H.*, et al.* (2012). Mutations in UVSSA cause UV-sensitive syndrome and impair RNA polymerase IIo

processing in transcription-coupled nucleotide-excision repair. Nat Genet *44*, 586-592.

Nakazawa, Y., Yamashita, S., Lehmann, A.R., and Ogi, T. (2010). A semi-automated non-radioactive system for measuring recovery of RNA synthesis and unscheduled DNA synthesis using ethynyluracil derivatives. DNA Repair (Amst) *9*, 506-516.

Nouspikel, T. (2011). Multiple roles of ubiquitination in the control of nucleotide excision repair. Mech Ageing Dev *132*, 355-365.

Odawara, J., Harada, A., Yoshimi, T., Maehara, K., Tachibana, T., Okada, S., Akashi, K., and Ohkawa, Y. (2011). The classification of mRNA expression levels by the phosphorylation state of RNAPII CTD based on a combined genome-wide approach. BMC Genomics *12*, 516.

Okuda, M., Nakazawa, Y., Guo, C., Ogi, T., and Nishimura, Y. (2017). Common TFIIH recruitment mechanism in global genome and transcription-coupled repair subpathways. Nucleic Acids Res *45*, 13043-13055.

Parmar, K., D'Andrea, A., and Niedernhofer, L.J. (2009). Mouse models of Fanconi anemia. Mutat Res *668*, 133-140.

Paulsen, M.T., Veloso, A., Prasad, J., Bedi, K., Ljungman, E.A., Magnuson, B., Wilson, T.E., and Ljungman, M. (2014). Use of Bru-Seq and BruChase-Seq for genome-wide assessment of the synthesis and stability of RNA. Methods *67*, 45-54.

Quinlan, A.R., and Hall, I.M. (2010). BEDTools: a flexible suite of utilities for comparing genomic features. Bioinformatics *26*, 841-842.

Rahl, P.B., Lin, C.Y., Seila, A.C., Flynn, R.A., McCuine, S., Burge, C.B., Sharp, P.A., and Young, R.A. (2010). c-Myc regulates transcriptional pause release. Cell *141*, 432-445.

Ran, F.A., Hsu, P.D., Wright, J., Agarwala, V., Scott, D.A., and Zhang, F. (2013) Genome engineering using the CRISPR-Cas9 system. Nat Protoc *8*, 2281-2308.

Ramirez, F., Dundar, F., Diehl, S., Gruning, B.A., and Manke, T. (2014). deepTools: a flexible platform for exploring deep-sequencing data. Nucleic Acids Res *42*, W187-191.

Ratner, J.N., Balasubramanian, B., Corden, J., Warren, S.L., and Bregman, D.B. (1998). Ultraviolet radiation-induced ubiquitination and proteasomal degradation of the large subunit of RNA polymerase II. Implications for transcription-coupled DNA repair. J Biol Chem *273*, 5184-5189.

Raudvere, U., Kolberg, L., Kuzmin, I., Arak, T., Adler, P., Peterson, H., and Vilo, J. (2019). g:Profiler: a web server for functional enrichment analysis and conversions of gene lists (2019 update). Nucleic Acids Res *47*, W191-W198.

Reid-Bayliss, K.S., Arron, S.T., Loeb, L.A., Bezrookove, V., and Cleaver, J.E. (2016). Why Cockayne syndrome patients do not get cancer despite their DNA repair deficiency. Proc Natl Acad Sci U S A *113*, 10151-10156.

Robinson, M.D., McCarthy, D.J., and Smyth, G.K. (2010). edgeR: a Bioconductor package for differential expression analysis of digital gene expression data. Bioinformatics *26*, 139-140.

Schwertman, P., Lagarou, A., Dekkers, D.H., Raams, A., van der Hoek, A.C., Laffeber, C., Hoeijmakers, J.H., Demmers, J.A., Fousteri, M., Vermeulen, W.*, et al.* (2012). UV-sensitive syndrome protein UVSSA recruits USP7 to regulate transcription-coupled repair. Nat Genet *44*, 598-602.

Shen, L., Shao, N., Liu, X., and Nestler, E. (2014). ngs.plot: Quick mining and visualization of next-generation sequencing data by integrating genomic databases. BMC Genomics *15*, 284.

Somesh, B.P., Reid, J., Liu, W.F., Sogaard, T.M., Erdjument-Bromage, H., Tempst, P., and Svejstrup, J.Q. (2005). Multiple mechanisms confining RNA polymerase II ubiquitylation to polymerases undergoing transcriptional arrest. Cell *121*, 913-923.

Somesh, B.P., Sigurdsson, S., Saeki, H., Erdjument-Bromage, H., Tempst, P., and Svejstrup, J.Q. (2007). Communication between distant sites in RNA polymerase II through ubiquitylation factors and the polymerase CTD. Cell *129*, 57-68.

Soucy, T.A., Smith, P.G., Milhollen, M.A., Berger, A.J., Gavin, J.M., Adhikari, S., Brownell, J.E., Burke, K.E., Cardin, D.P., Critchley, S.*, et al.* (2009). An inhibitor of NEDD8-activating enzyme as a new approach to treat cancer. Nature *458*, 732-736.

Starita, L.M., Horwitz, A.A., Keogh, M.C., Ishioka, C., Parvin, J.D., and Chiba, N. (2005). BRCA1/BARD1 ubiquitinate phosphorylated RNA polymerase II. J Biol Chem *280*, 24498-24505.

Storey, J.D., and Tibshirani, R. (2003). Statistical significance for genomewide studies. Proc Natl Acad Sci U S A *100*, 9440-9445.

Sugaya, K., Vigneron, M., and Cook, P.R. (2000). Mammalian cell lines expressing functional RNA polymerase II tagged with the green fluorescent protein. J Cell Sci *113*, 2679-2683.

Thorvaldsdottir, H., Robinson, J.T., and Mesirov, J.P. (2013). Integrative Genomics Viewer (IGV): high-performance genomics data visualization and exploration. Brief Bioinform *14*, 178-192.

Tischler, G., and Leonard, S. (2014). biobambam: tools for read pair collation based algorithms on BAM files. Source Code for Biology and Medicine *9*, 13. https://doi.org/10.1186/1751-0473-9-13

van der Horst, G.T., van Steeg, H., Berg, R.J., van Gool, A.J., de Wit, J., Weeda, G., Morreau, H., Beems, R.B., van Kreijl, C.F., de Gruijl, F.R.*, et al.* (1997). Defective transcription-coupled repair in Cockayne syndrome B mice is associated with skin cancer predisposition. Cell *89*, 425-435.

van der Pluijm, I., Garinis, G.A., Brandt, R.M., Gorgels, T.G., Wijnhoven, S.W., Diderich, K.E., de Wit, J., Mitchell, J.R., van Oostrom, C., Beems, R.*, et al.* (2007). Impaired genome maintenance suppresses the growth hormone--insulin-like growth factor 1 axis in mice with Cockayne syndrome. PLoS Biol *5*, e2.

van der Weegen, Y., H.G. Berman, T.E.T. Mevissen, K. Apelt, R. González-Prieto, E. Heilbrun, A.C.O. Vertegaal, D. van den Heuvel, J.C. Walter, S. Adar, and M.S. Luijsterburg. 2019. The sequential and cooperative action of CSB, CSA and UVSSA targets the TFIIH complex to DNA damage-stalled RNA polymerase II. https://www.biorxiv.org/content/10.1101/707216v1

Wang, Y., Chakravarty, P., Ranes, M., Kelly, G., Brooks, P.J., Neilan, E., Stewart, A., Schiavo, G., and Svejstrup, J.Q. (2014). Dysregulation of gene expression as a cause of Cockayne syndrome neurological disease. Proc Natl Acad Sci U S A *111*, 14454-14459.

1 Watson, A.T., Garcia, V., Bone, N., Carr, A.M., and Armstrong, J. (2008). Gene
2 tagging and gene replacement using recombinase-mediated cassette exchange
3 in Schizosaccharomyces pombe. Gene *407*, 63-74.

4 Woudstra, E.C., Gilbert, C., Fellows, J., Jansen, L., Brouwer, J., Erdjument-
5 Bromage, H., Tempst, P., and Svejstrup, J.Q. (2002). A Rad26-Def1 complex
6 coordinates repair and RNA pol II proteolysis in response to DNA damage.
7 Nature *415*, 929-933.

8 Xu, J., Lahiri, I., Wang, W., Wier, A., Cianfrocco, M.A., Chong, J., Hare, A.A.,
9 Dervan, P.B., DiMaio, F., Leschziner, A.E.*, et al.* (2017). Structural basis for the
10 initiation of eukaryotic transcription-coupled DNA repair. Nature *551*, 653-657.

11 Yamaizumi, M., and Sugano, T. (1994). U.v.-induced nuclear accumulation of
12 p53 is evoked through DNA damage of actively transcribed genes independent
13 of the cell cycle. Oncogene *9*, 2775-2784.

14 Yasukawa, T., Kamura, T., Kitajima, S., Conaway, R.C., Conaway, J.W., and
15 Aso, T. (2008). Mammalian Elongin A complex mediates DNA-damage-induced
16 ubiquitylation and degradation of Rpb1. EMBO J *27*, 3256-3266.

17 Zhang, X., Horibata, K., Saijo, M., Ishigami, C., Ukai, A., Kanno, S., Tahara, H.,
18 Neilan, E.G., Honma, M., Nohmi, T.*, et al.* (2012). Mutations in UVSSA cause
19 UV-sensitive syndrome and destabilize ERCC6 in transcription-coupled DNA
20 repair. Nat Genet *44*, 593-597.

Figure 1

Click here to access/download;Figure;NakazawaFig1R3.tiff

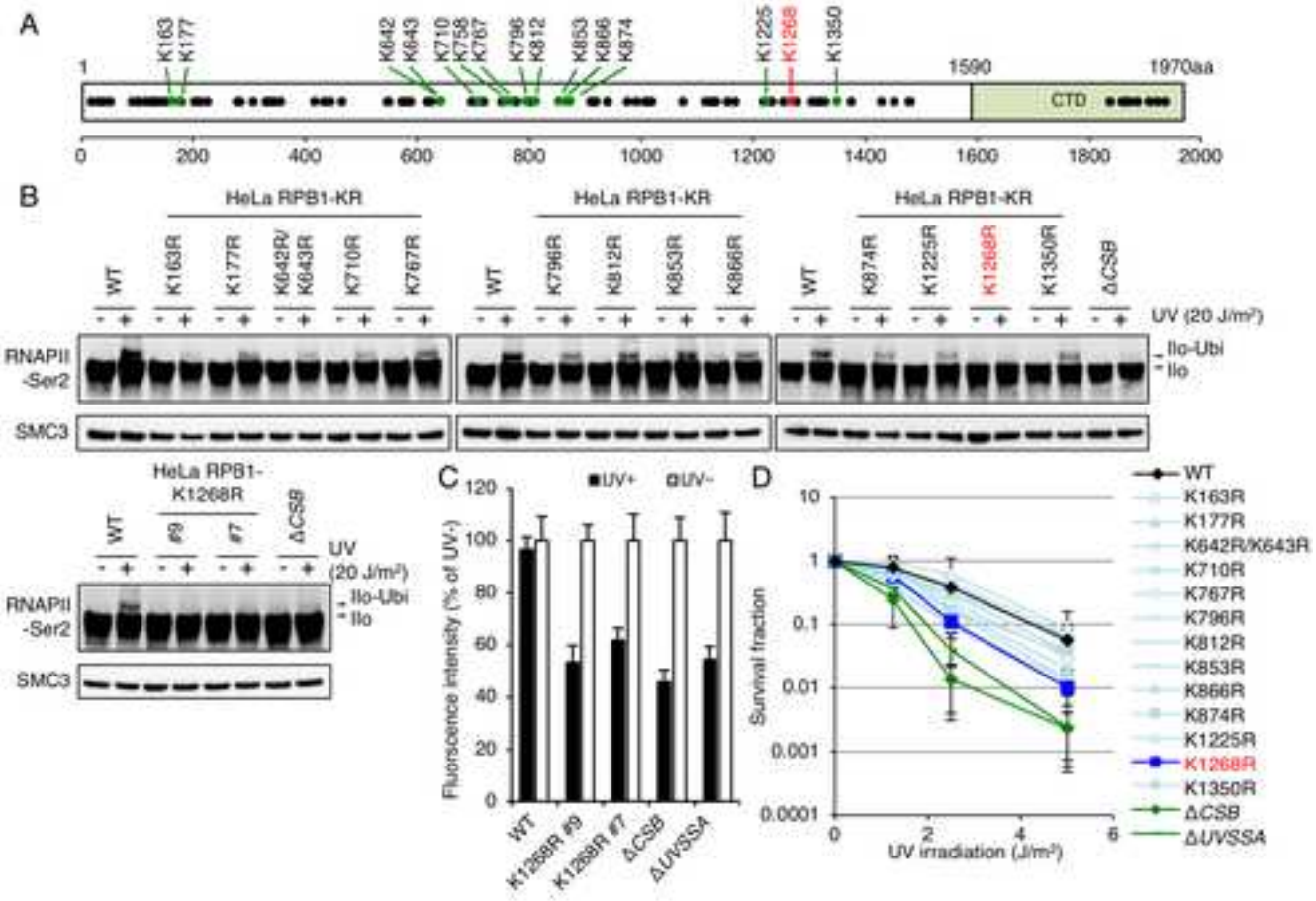

Fig1

Figure 2

Click here to access/download;Figure;NakazawaFig2R3.tiff

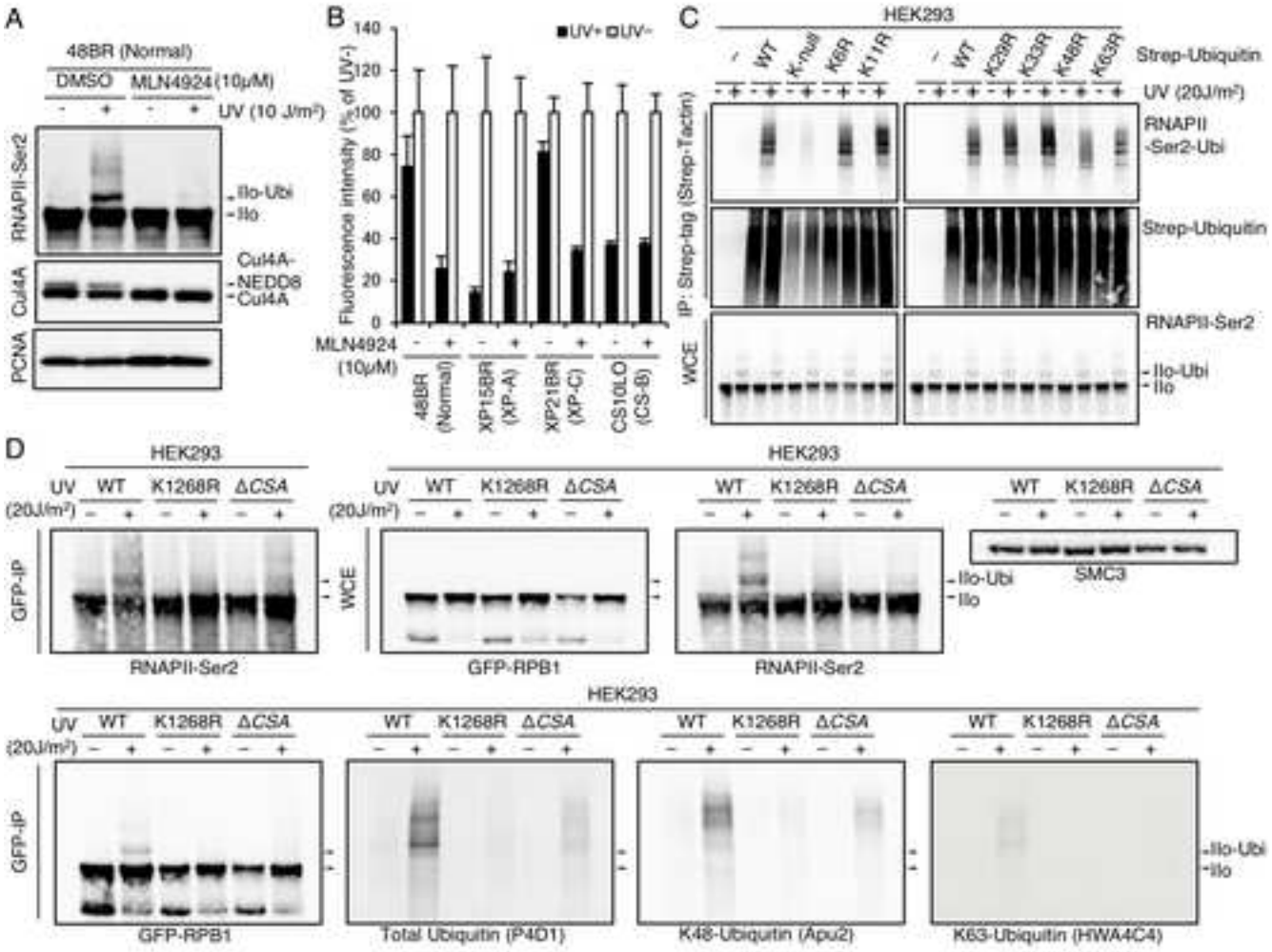

Fig2

Figure 3

Click here to access/download;Figure;NakazawaFig3R3.tiff

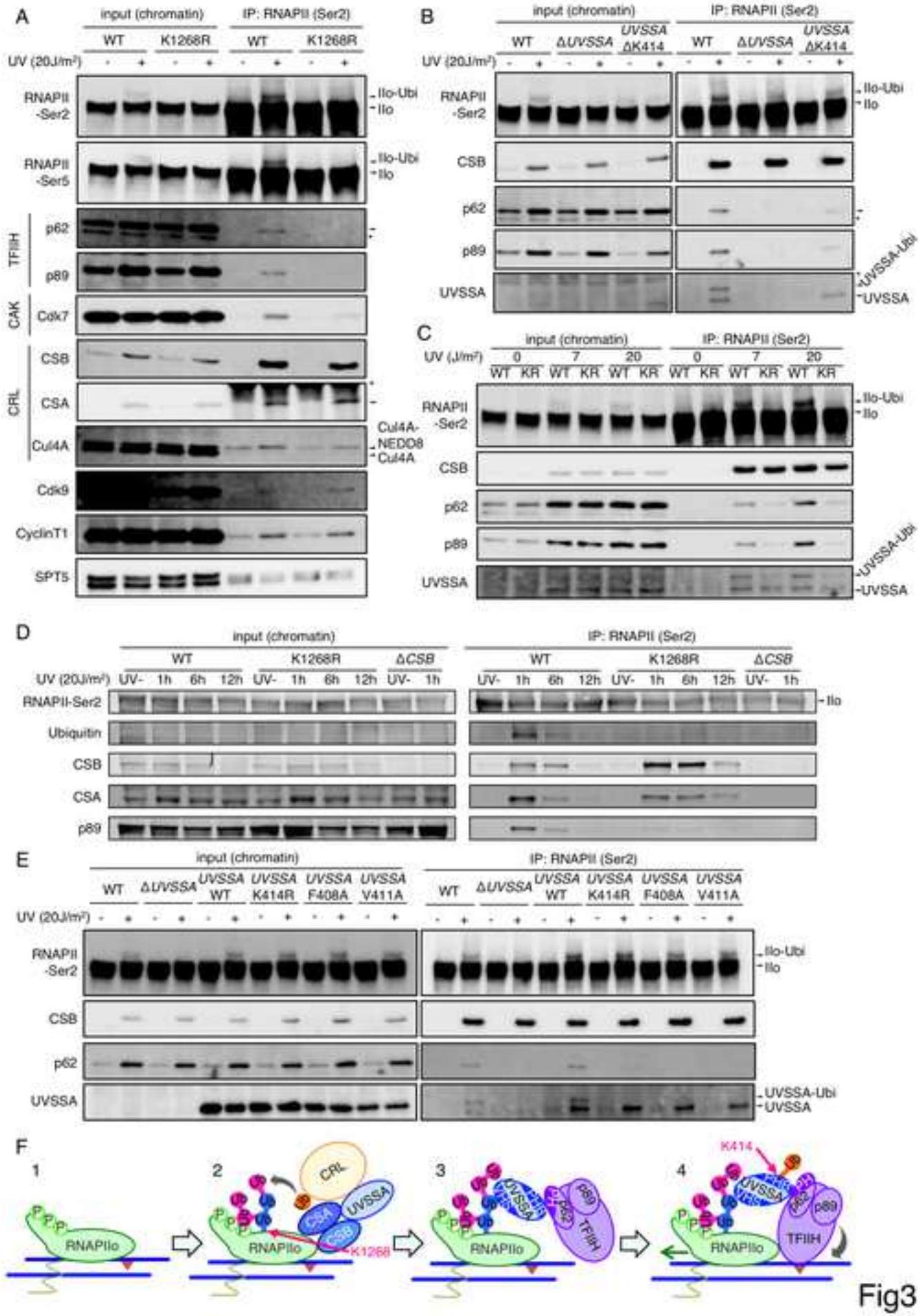

Fig3

Figure 4

Click here to access/download;Figure;NakazawaFig4R1.tiff

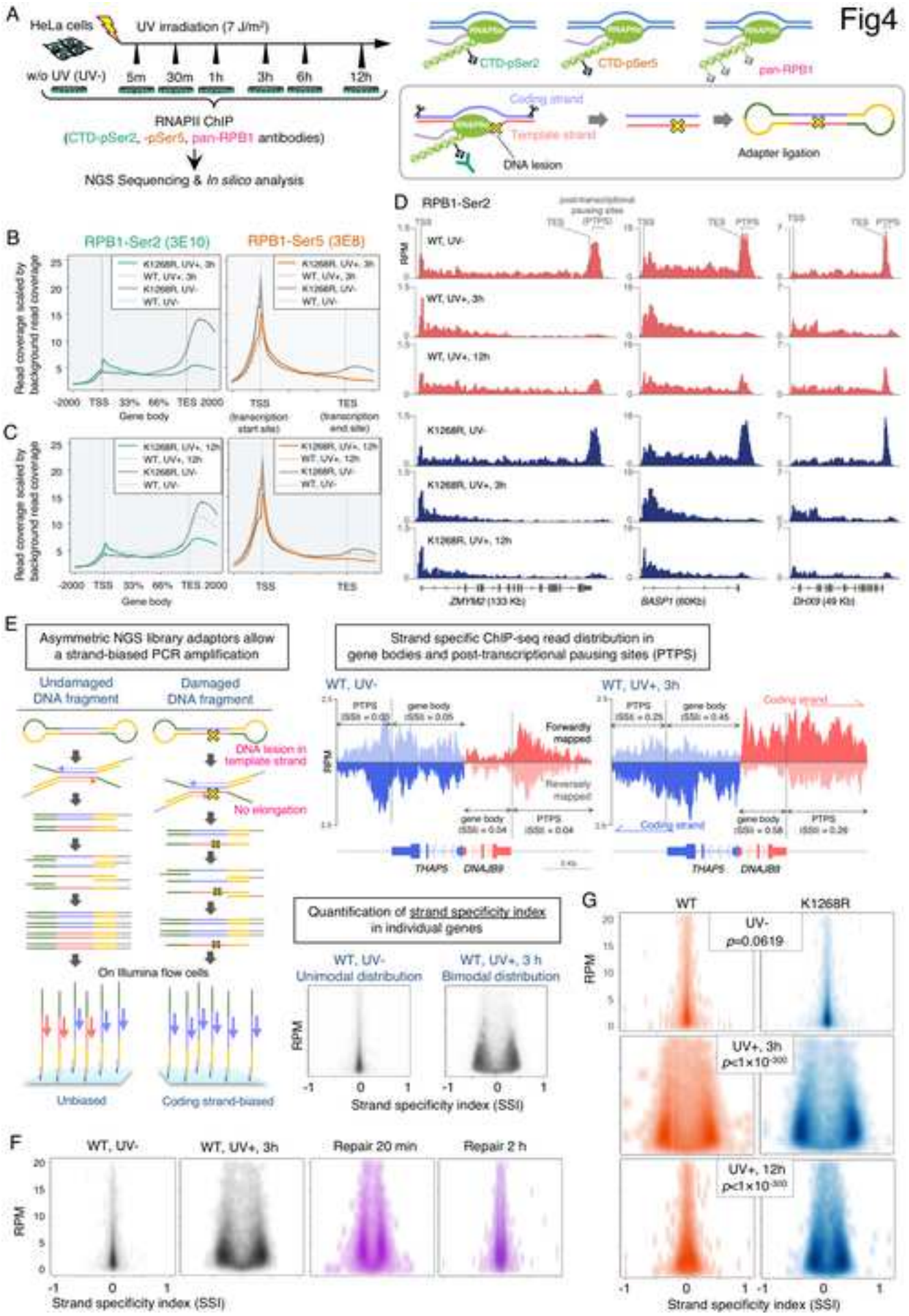

Figure 5

Click here to access/download;Figure;NakazawaFig5R1.tiff

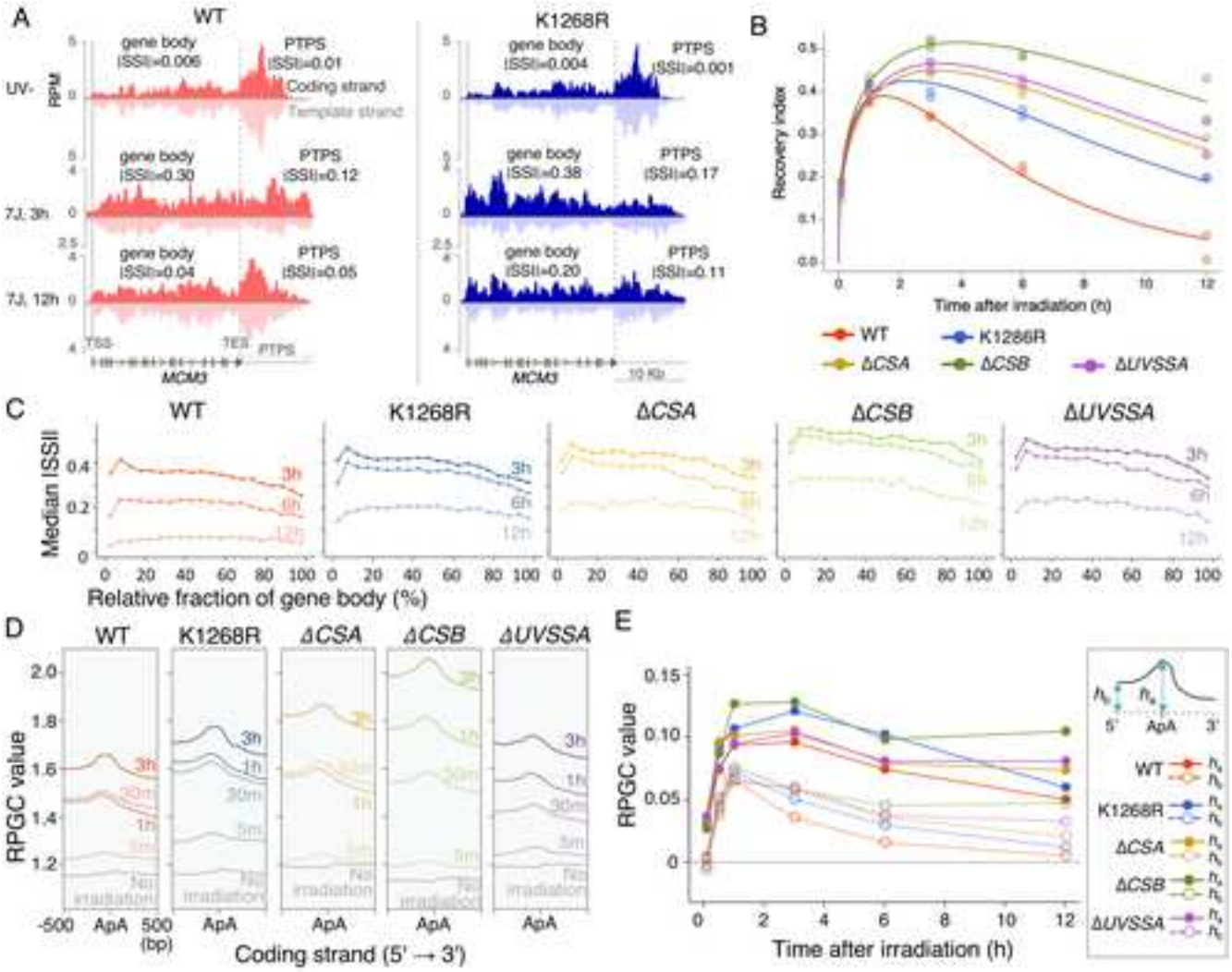

Fig5

Figure 6

Click here to access/download;Figure;NakazawaFig6R3.tiff

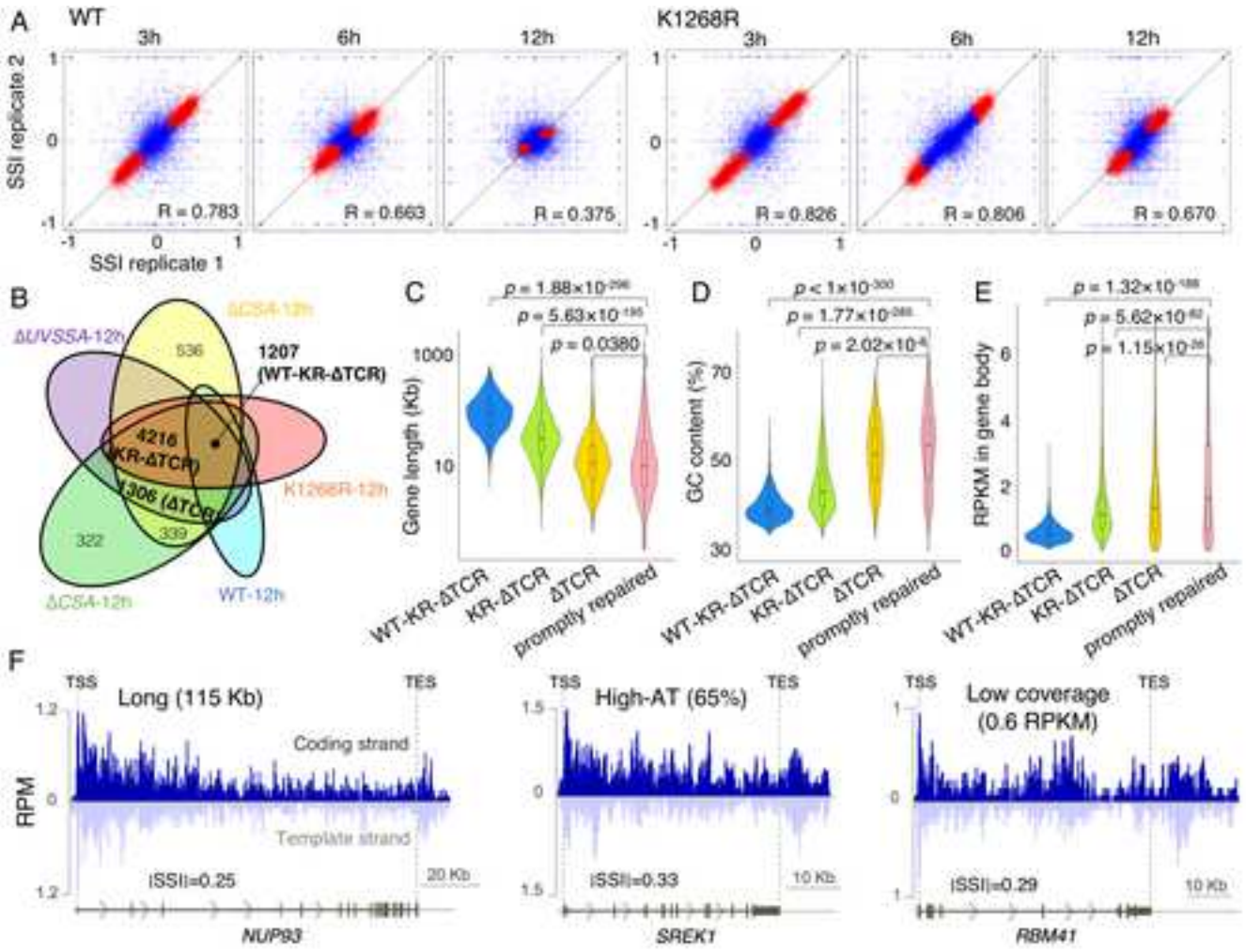

Fig6

Figure 7

Click here to access/download;Figure;NakazawaFig7R3.tiff

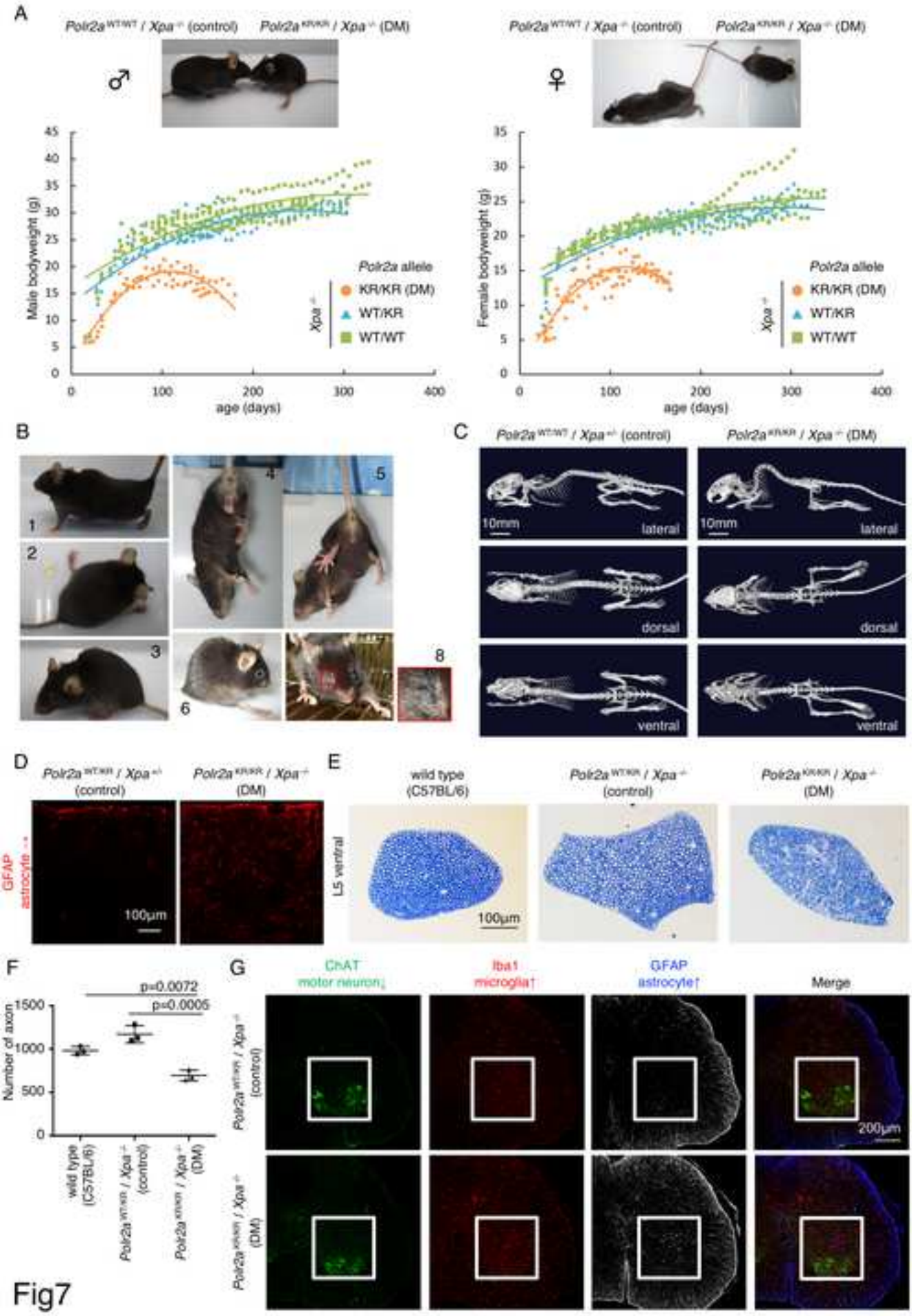

Table S1 SILAC differential mass-spectrometry identified RPB1-K1268 ubiquitination in UV-irradiated cells (1 h, 10 J/m^2), Related to Figure 1

Annotated Sequence in RPB1 (P24928)	Qvality PEP	Qvality *q*-value	# PSMs	Positions	# Missed Cleavages	Theoretical MH+ (Da)	Abundances (scaled) (WT)	Abundances (scaled) (Δ*UVSSA*)	Abundance Ratio* (Δ*UVSSA*) / (WT)
IMNSDEN(**K**)MQEEEEVVDKMDDDVFLR (1xGG [K8])	9.5698×10^{-8}	0	4	1261-1286	2	3272.43918	177.8	22.2	0.125

*SILAC ratio. Ubiquitinated lysine residue is indicated by boldface. WT, HCT116 wild-type cells; Δ*UVSSA*, *UVSSA*-deleted HCT116 cells.

Table S2 Mass-spectrometry identified RPB1-K1268 ubiquitination after UV irradiation (1 h, 20 J/m^2), Related to Figure 1

Positions in RPB1 (P24928)	Intensity (Replicate. 1)	Intensity (Replicate. 2)	GlyGly (K) probabilities in detected peptides*	Modifications
163	4285100	0	NICEGGEEMDN**K** (1)FGVEQPEGDEDLTK	1xGG [K12]
177	13760000	0	FGVEQPEGDEDLT**K** (0.869)EK (0.131)	1xGG [K14]
758	1949200	0	TGSSAQ**K** (0.996)SLSEYNNFK (0.004)	1xGG [K7]
853	0	1245900	EGLIDTAV**K** (1)TAETGYIQR	1xGG [K9]
1268	20479000	10857000	IMNSDEN**K** (1)MQEEEEVVDK	1xGG [K8], Oxidation [M2]
1350	2449300	0	VLSE**K** (1)DVDPVR	1xGG [K5]

*Ubiquitinated lysine residue is indicated by boldface. Probabilities of ubiquitination for each lysine residue were shown in parentheses. Wild-type HeLa cells were UV irradiated.

Table S3 CRISPR/Cas9-based gene editing and cell lines used in this study, Related to Figure 1 and STAR Methods

Cell line	CRISPR/Cas9 guide RNA (gRNA)	Homology directed repair (HDR) oligos	clone # used in this study
(1) HCT116 Δ*UVSSA* cell line			
Δ*UVSSA*	GTGTGGAGGT CCCTGAGAAG G	-	# 1
(2) HeLa RPB1-KR mutants			
RBP1-K163R	GATGGACAAC AAGTTCGGTG	CCTCCAGGCCTCTGACCCCTCCTTCCCA AAAGTCTCCGCCAGCCCCAGCCACCTTT TCTTTGGTCAGATCCTCGTCACCCTCAG GTTGTTC[**g****]ACACCGAAC[**C***]TGTTGTC CATCTCCTCCCCACCCTCGCATATGTTTT T	# 4
RBP1-K177R	GGATCTGACC AAAGAAAAGG	CCAGCCCCTCCTGTTTCCTTCCCTTCCAG TTTCCTCCCTCCAGGCCTCTGACCCCTCC TTCCCAAAAGTCTCCGCCAGCCCCAGCC ACCTT[**c****]TCT[**C***]TGGTCAGATCCTCGT CACCCTCAGGTTGTTCCACACC	# 8
RBP1-K642R/ K643R	GTGCCCAGAG ACTTCTTACAC	ATTTGGACGTGGGAGCCAGGACCAGAG CAGGGGCCTTGAGTGGGTGCTTTGTCCT TAGGTGGTGGTGGAGAATGGGGAGCTG ATCATGGGCAT[**t****]CTGTGTA[**G***]GA[**G***] GTCTCTGGGCACGTCAGCTGGCTCCCTG GTCCACATC	# 16
RBP1-K710R	GCACTATTAA GAAGGCCAAG C	ACTCCCTTTGCTCTTGATGATGCTAACTT CGAAGTCCCTGGAAACCCCTTATTCCGT CTCTGGTGGCCTCCCCTCTTACCTCTATT ACGTC[**t****]TGC[**C***]TGGCCTTCTTAATAG TGTTCTGAATGTCCTGGTAAGT	# 23
RBP1-K767R	GTTCAAGTCTA TGGTCGTGTC	TCCTTCCTCCTCCCAAACTTCACAGCGG CCCCGTATATGGAAAAACAAGGCTTCTC ACCTGGGAGATGTTAATCTTGGAACCTT TAGCTCCG[**ctg****]ACGACCATAGAC[**C***]T GAAGTTATTGTATTCAGACAGGGATTTC TGAGCAGA	# 2
RBP1-K796R	GAGCAGAACG TCGAGGGCAA G	GGTAGGAGTTCTCCACAAAGCCACGGCT CTCAGGCCCGTAGTCATCCTTGATGAAG TGAGGCAGAGTCCGGTGCTTGAAGCCA AATGGAAT[**t****]C[**t****]C[**C***]TGCCCTCGAC GTTCTGCTGTCCAACGACAGCAATGAC	# 14
RBP1-K812R	GACTCTGCCTC ACTTCATCA	CCCCCATGGCGTGGAAAAAGAACTCAG TGGGTGTGAGGCCGGCTAGGTAGGAGT TCTCCACAAAGCCACGGCTCTCAGGCCC GTAGTCATC[**t******C***]TGATGAAGTGAGGCA GAGTCCGGTGCTTGAAGCCAAA	# 32
RBP1-K853R	GCTGTCAAGA CTGCTGAGAC	GAGCATTTCCGCTCCCCACCTGTTAGGG GTTTCTCAGCCTGCAGCAGTCCCTGCTA ACAGCCCAAGGAAGACCCCTGAGGAAA	# 29

		GCCTCACC[**g****]GT[**t****]TCAGCAGTC[**C***]TGACAGCCGTGTCAATGAGCCCCTCACGACCCCCCAT	
RBP1-K866R	GCGGCGGCTGATCAAGTCCA	CCAGGCCGTCTTCGCCGTAGCGCAGCTGCACCACCTGGTTGATGGAGTTCCGCACAGTCGCGTCGTACTTCACCATCACTGACTCCATGGAC[**C***]TGATCAGCC[**t****]CCGCTGGATGTATCCTGGAGGGAAGTAAGGGGATGA	# 3
RBP1-K874R	GTGAAGTACGACGCGACTGTG	GCTTAAGCGTAGCCAGGTTCTGGAACTCAACGCTCTCGCCTGCCAGGCCGTCTTCGCCGTAGCGCAGCTGCACCACCTGGTTGATGGAGTT[**t****]C[**t****]CACAGTCGCGTCGTAC[**C***]TCACCATCACTGACTCCATGGACTTGATCAGCCGCCG	# 4
RBP1-K1225R	GACTGACCGGAAGCTCACCA	ACGATAGGTGGTAGCCCAGAGAGCGGGGCTCCTGAGCCAGGCCAGCCCTCCTAGGCTTACCAGCATTGATCTTTTCAGCAATCTGCTCCAT[**t****]GT[**c****]A[**a****]C[**C***]TCCGGTCAGTCATGTGCTTCCGATCCAGCTCCACCCG	# 21
RBP1-K1268R	GCGATGAGAACAAGATGCAAG	AGGTTTTGGTGACGACTTGAACTGCATCTTTAATGATGACAATGCAGAGAAGCTGGTGCTCCGTATTCGCATCATGAACAGCGATGAGAACA[**G***]GATGCAAGAGGTAATGGGGGTCCTAGAAGTCAGCGTG	# 7 (Fig. 1B, 1C), # 9 (all Figs.)
RBP1-K1350R	GGTGCTGAGTGAGAAGGACG	AGCCAGAGATCCACGAAAGGCAGCTAGGCAGCACACACGGGCTCACCGTGAAGATCTCCACAATGTCATTGGACGTGGTGCGTACGGGGTC[**g****]ACGTC[**t******C***]TCTCACTCAGCACCCGCATCAAGCTCACGCCGTCCGT	# 8

(3) HeLa ΔTCR mutants

Δ*CSA*	GTCCGCACGCCAAACGGGTT	-	# 5
Δ*CSB*	GCTTCTCCACGTCAACGAGCT	-	# 1
Δ*UVSSA*, UVSSA-ΔK414	GTGTGGAGGTCCCTGAGAAGG	-	# 5 # 1

(4) HEK293 GFP-RPB1 expressing cell lines

RPB1-WT***	GCCTGCCTCCGCCATGCACG	-	# 1
RPB1-K1268R***		-	# 7
RPB1-WT, Δ*CSA****	same as above	-	# 13

*Lys->Arg target mutations; **silent mutations (lower cases). ***endogenous *POLR2A* alleles were deleted.

Table S4 *Polr2a*$^{K1268R/K1268R}$ single mutant mice phenotype, Related to Figure 7

Parameter	Sex	Age (days)	*Polr2a*$^{WT/WT}$	*Polr2a*$^{WT/KR}$	*Polr2a*$^{KR/KR}$	*p*-value*	Remarks
Bodyweight (g)	♂	80±5	27.0±1.8 (6)	26.5±1.7 (6)	26.9±2.1 (10)	1.00	
		110±5	28.0±2.1 (6)	28.3±2.0 (6)	28.4±2.3 (10)	1.00	
		130±5	29.3±2.2 (6)	29.0±2.6 (6)	29.3±2.6 (10)	1.00	
	♀	80±5	19.9±1.1 (7)	20.3±1.1 (16)	20.1±1.4 (8)	0.866	
		110±5	20.9±0.92 (7)	21.2±1.2 (16)	21.5±1.2 (8)	0.866	
		130±5	21.3±1.1 (7)	21.7±0.97 (16)	21.8±1.1 (8)	0.866	
Fertility	♂+♀	60->365	Normal	Normal	Normal		
Gait abnormalities	♂+♀	90->365	-	-	-		
Hind limb dystonia	♂+♀	20->365	-	-	-		Results from a tail suspension test.
Kyphosis	♂+♀	90->365	-	-	-		

Values are average ± S.D; number of tested animals are shown in parentheses. **P*-values were calculated to test the difference in bodyweights between *Polr2a*$^{WT/WT}$ vs *Polr2a*$^{KR/KR}$ animals with the Mann-Whitney *U*-test, and were corrected by the Benjamini-Hochberg method. WT, wild type; KR, K1268R.

Table S5 *Polr2a*$^{K1268R/K1268R}$ / *Xpa*$^{+/-}$ mice phenotype (*Xpa* heterozygous deletion), Related to Figure 7

Parameter	Sex	Age (days)	*Polr2a*$^{WT/WT}$ / *Xpa*$^{+/-}$	*Polr2a*$^{WT/KR}$ / *Xpa*$^{+/-}$	*Polr2a*$^{KR/KR}$ / *Xpa*$^{+/-}$	*p*-value*	Remarks
Bodyweight (g)	♂	80±5	24.5±1.4 (5)	24.9±1.5 (8)	26.0±1.2 (12)	0.172	
		110±5	26.6±0.84 (4)	27.4±1.1 (10)	27.8±1.3 (6)	0.240	
		150±7	27.7±2.3 (4)	29.0±1.2 (6)	29.1±1.2 (6)	0.202	
		260±10	32 (1)	32.2±2.1 (4)	33.6±1.1 (2)	NA	
	♀	80±5	19.6±1.2 (6)	20.1±0.87 (12)	20.7±0.0 (2)	0.241	
		110±5	20.7±0.65 (4)	21.6±0.85 (12)	25.1 (1)	NA	
		150±7	22.1±1.57 (3)	22.4±1.0 (9)	NA	NA	
Fertility	♂+♀	60->365	Normal	Normal	Normal		
Gait abnormalities	♂+♀	90->365	-	-	-		
Hind limb dystonia	♂+♀	20->365	-	-	-		Results from a tail suspension test.
Kyphosis	♂+♀	90->365	-	-	-		

Values are average ± S.D; number of tested animals are shown in parentheses. **P*-values were calculated to test the difference in bodyweights between *Polr2a*$^{WT/WT}$ / *Xpa*$^{+/-}$ vs *Polr2a*$^{KR/KR}$ / *Xpa*$^{+/-}$ animals with the Mann-Whitney *U*-test, and were corrected by the Benjamini-Hochberg method. WT, wild type; KR, K1268R.

Table S6 DM mice phenotype, Related to Figure 7

Parameter	Sex	Age (days)	*Polr2a*$^{WT/WT}$ / *Xpa*$^{-/-}$	*Polr2a*$^{WT/KR}$ / *Xpa*$^{-/-}$	*Polr2a*$^{KR/KR}$ / *Xpa*$^{-/-}$ (DM)	*p*-value*	Remarks
Bodyweight (g)	♂	80±5	26.2±1.3 (9)	22.5±3.4 (22)	18.5±2.4 (4)	0.00952	Differences between WT/WT and WT/K1268R are also statistically significant in male mice (< 160 days).
		110±5	27.9±1.2 (6)	24.2±2.8 (10)	18.2±1.6 (4)	0.00952	
		150±7	28.9±1.5 (8)	26.5±2.1 (12)	16.2±1.3 (5)	0.00466	
		275±5	32.5±3.3 (3)	31.2±0.75 (3)	NA	NA	
	♀	80±5	19.0±1.1 (11)	19.3±1.0 (16)	14.8±2.0 (4)	0.000754	
		110±5	20.7±0.8 (12)	20.7±0.9 (16)	14.9±2.0 (4)	0.00435	
		150±7	21.4±0.7 (10)	21.6±1.0 (14)	14.8±0.8 (5)	0.00401	
		275±5	25.5±3.6 (4)	23.8±1.5 (7)	NA	NA	
Fertility	♂+♀	60->365	Normal	Normal	Not Tested		
Gait abnormalities	♂+♀	90	-	-	Moderate		
		120-180	-	-	Prominent		
Hind limb dystonia	♂+♀	20-180	-	-	+		Results from a tail suspension test.
Kyphosis	♂+♀	90	-	-	Moderate		
		150-180	-	-	Prominent		
Depigmentation (animals)	♂+♀	90-180	0 (21)	0 (40)	2 (12)		
Cataract (animals)	♂+♀	90-180	0 (21)	0 (40)	2 (12)		Monocular cases.

Values are average ± S.D; number of tested animals are shown in parentheses. **P*-values were calculated to test the difference in bodyweights between *Polr2a*$^{WT/WT}$ / *Xpa*$^{-/-}$ vs *Polr2a*$^{KR/KR}$ / *Xpa*$^{-/-}$ (DM) animals with the Mann-Whitney *U*-test, and were corrected by the Benjamini-Hochberg method. WT, wild type; KR, K1268R.

Table S7 ChIP-seq data summary, Related to STAR Methods

Cell type (Hela Mutant)	UV (J/m2)	Time after irradiation	Antibody	Replicate number	SRA Run ID	Analysis in which sequence data were used						
						ngsplot	SSI-scatter	SSI-RI	T-T site	replicate-check	SSI difference	PreCR
						Fig. 4B, 4C, S4A, S4B	Fig. 4G, S4E	Fig. 5B, 5C, S5B-D	Fig. 5D, 5E, S5E, S5F	Fig. S4D	Fig. 6A-E, S6A	Fig. 4F
RPB1-K1268R	0	0h	3E10	1	SRR9722058	✓	✓		✓	✓		
RPB1-K1268R	0	0h	3E10	2	SRR9722057					✓		
RPB1-K1268R	7	5m	3E10	1	SRR9722060	✓	✓	✓	✓			
RPB1-K1268R	7	30m	3E10	1	SRR9722059	✓						
RPB1-K1268R	7	1h	3E10	1	SRR9722062	✓	✓	✓	✓	✓		
RPB1-K1268R	7	1h	3E10	2	SRR9722061			✓		✓		
RPB1-K1268R	7	3h	3E10	1	SRR9722064			✓		✓	✓	
RPB1-K1268R	7	3h	3E10	2	SRR9722063	✓	✓	✓	✓	✓	✓	
RPB1-K1268R	7	6h	3E10	1	SRR9722056	✓	✓	✓	✓			
RPB1-K1268R	7	6h	3E10	2	SRR9722055			✓				
RPB1-K1268R	7	12h	3E10	1	SRR9722145	✓	✓	✓	✓	✓	✓	
RPB1-K1268R	7	12h	3E10	2	SRR9722144			✓		✓	✓	
RPB1-K1268R	7	12h	3E10	3	SRR9722143						✓	
WT	0	0h	3E10	1	SRR9722142	✓	✓		✓	✓		
WT	0	0h	3E10	2	SRR9722156					✓		
WT	7	5m	3E10	1	SRR9722155	✓	✓	✓	✓			
WT	7	30m	3E10	1	SRR9722147	✓						
WT	7	1h	3E10	1	SRR9722146	✓	✓	✓	✓	✓		
WT	7	1h	3E10	2	SRR9722158			✓		✓		
WT	7	3h	3E10	1	SRR9722157			✓		✓	✓	
WT	7	3h	3E10	2	SRR9722079	✓	✓	✓	✓	✓	✓	
WT	7	6h	3E10	1	SRR9722080	✓	✓	✓	✓			
WT	7	6h	3E10	2	SRR9722077			✓				
WT	7	12h	3E10	1	SRR9722078	✓	✓	✓	✓	✓	✓	
WT	7	12h	3E10	2	SRR9722083			✓		✓	✓	
WT	7	12h	3E10	3	SRR9722084						✓	
WT	7	12h	3E10	4	SRR9722081						✓	
ΔCSA	0	0h	3E10	1	SRR9722082	✓	✓		✓	✓		
ΔCSA	0	0h	3E10	2	SRR9722075					✓		
ΔCSA	7	5m	3E10	1	SRR9722076	✓	✓	✓	✓			
ΔCSA	7	30m	3E10	1	SRR9722068	✓						
ΔCSA	7	1h	3E10	1	SRR9722067	✓	✓	✓	✓	✓		

ΔCSA	7	1h	3E10	2	SRR9722070			✓		✓		
ΔCSA	7	3h	3E10	1	SRR9722069	✓	✓	✓	✓	✓	✓	
ΔCSA	7	3h	3E10	2	SRR9722072			✓		✓	✓	
ΔCSA	7	6h	3E10	1	SRR9722071	✓	✓	✓	✓			
ΔCSA	7	6h	3E10	2	SRR9722074			✓				
ΔCSA	7	12h	3E10	1	SRR9722073	✓	✓	✓	✓	✓	✓	
ΔCSA	7	12h	3E10	2	SRR9722066			✓		✓	✓	
ΔCSB	0	0h	3E10	1	SRR9722065	✓	✓		✓	✓		
ΔCSB	0	0h	3E10	2	SRR9722097					✓		
ΔCSB	7	5m	3E10	1	SRR9722098	✓	✓	✓	✓			
ΔCSB	7	30m	3E10	1	SRR9722099	✓						
ΔCSB	7	1h	3E10	1	SRR9722100	✓	✓	✓	✓	✓		
ΔCSB	7	1h	3E10	3	SRR9722101			✓		✓		
ΔCSB	7	3h	3E10	1	SRR9722102	✓	✓	✓	✓	✓	✓	
ΔCSB	7	3h	3E10	3	SRR9722103			✓		✓	✓	
ΔCSB	7	6h	3E10	1	SRR9722104	✓	✓	✓	✓			
ΔCSB	7	6h	3E10	2	SRR9722095			✓				
ΔCSB	7	12h	3E10	1	SRR9722096	✓	✓	✓	✓	✓	✓	
ΔCSB	7	12h	3E10	2	SRR9722094			✓		✓	✓	
ΔUVSSA	0	0h	3E10	1	SRR9722093	✓	✓		✓	✓		
ΔUVSSA	0	0h	3E10	2	SRR9722092					✓		
ΔUVSSA	7	30m	3E10	1	SRR9722090	✓	✓		✓			
ΔUVSSA	7	5m	3E10	1	SRR9722091	✓		✓				
ΔUVSSA	7	1h	3E10	1	SRR9722089	✓	✓	✓	✓	✓		
ΔUVSSA	7	1h	3E10	2	SRR9722088			✓		✓		
ΔUVSSA	7	3h	3E10	1	SRR9722087	✓	✓	✓	✓	✓	✓	
ΔUVSSA	7	3h	3E10	2	SRR9722086			✓		✓	✓	
ΔUVSSA	7	6h	3E10	1	SRR9722085	✓	✓	✓	✓			
ΔUVSSA	7	6h	3E10	2	SRR9722121			✓				
ΔUVSSA	7	12h	3E10	1	SRR9722122	✓	✓	✓	✓	✓	✓	
ΔUVSSA	7	12h	3E10	2	SRR9722119			✓		✓	✓	
ΔCSA	0	0h	3E8	1	SRR9722120	✓						
ΔCSA	7	3h	3E8	1	SRR9722117	✓						
ΔCSA	7	6h	3E8	1	SRR9722118	✓						
ΔCSA	7	12h	3E8	1	SRR9722115	✓						
ΔCSB	0	0h	3E8	1	SRR9722116	✓						
ΔCSB	7	3h	3E8	1	SRR9722123	✓						
ΔCSB	7	6h	3E8	1	SRR9722124	✓						
ΔCSB	7	12h	3E8	1	SRR9722110	✓						

ΔUVSSA	0	0h	3E8	1	SRR9722109	✓						
ΔUVSSA	7	3h	3E8	1	SRR9722112	✓						
ΔUVSSA	7	6h	3E8	1	SRR9722111	✓						
ΔUVSSA	7	12h	3E8	1	SRR9722106	✓						
RPB1-K1268R	0	0h	3E8	1	SRR9722105	✓						
RPB1-K1268R	7	3h	3E8	1	SRR9722108	✓						
RPB1-K1268R	7	6h	3E8	1	SRR9722107	✓						
RPB1-K1268R	7	12h	3E8	1	SRR9722114	✓						
WT	0	0h	3E8	1	SRR9722113	✓						
WT	7	3h	3E8	1	SRR9722152	✓						
WT	7	6h	3E8	1	SRR9722153	✓						
WT	7	12h	3E8	1	SRR9722154	✓						
ΔCSA	0	0h	A304-405A	1	SRR9722052	✓						
ΔCSA	7	3h	A304-405A	1	SRR9722148	✓						
ΔCSA	7	6h	A304-405A	1	SRR9722149	✓						
ΔCSA	7	12h	A304-405A	1	SRR9722150	✓						
ΔCSB	0	0h	A304-405A	1	SRR9722151	✓						
ΔCSB	7	3h	A304-405A	1	SRR9722053	✓						
ΔCSB	7	6h	A304-405A	1	SRR9722054	✓						
ΔCSB	7	12h	A304-405A	1	SRR9722137	✓						
ΔUVSSA	0	0h	A304-405A	1	SRR9722136	✓						
ΔUVSSA	7	3h	A304-405A	1	SRR9722135	✓						
ΔUVSSA	7	6h	A304-405A	1	SRR9722134	✓						
ΔUVSSA	7	12h	A304-405A	1	SRR9722141	✓						
RPB1-K1268R	0	0h	A304-405A	1	SRR9722140	✓						
RPB1-K1268R	7	3h	A304-405A	1	SRR9722139	✓						
RPB1-K1268R	7	6h	A304-405A	1	SRR9722138	✓						
RPB1-K1268R	7	12h	A304-405A	1	SRR9722133	✓						
WT	0	0h	A304-405A	1	SRR9722132	✓						
WT	7	3h	A304-405A	1	SRR9722127	✓						
WT	7	6h	A304-405A	1	SRR9722128	✓						
WT	7	12h	A304-405A	1	SRR9722125	✓						
WT	7	0h	ab5095	1	SRR9722129							✓
WT	7	3h	ab5095	1	SRR9722126							✓
WT + PreCR-20min	7	3h	ab5095	1	SRR9722131							✓
WT + PreCR-2h	7	3h	ab5095	1	SRR9722130							✓

The sequence data were deposited in the NCBI Short Read Archive (SRA), with the BioProject accession number, PRJNA548234.

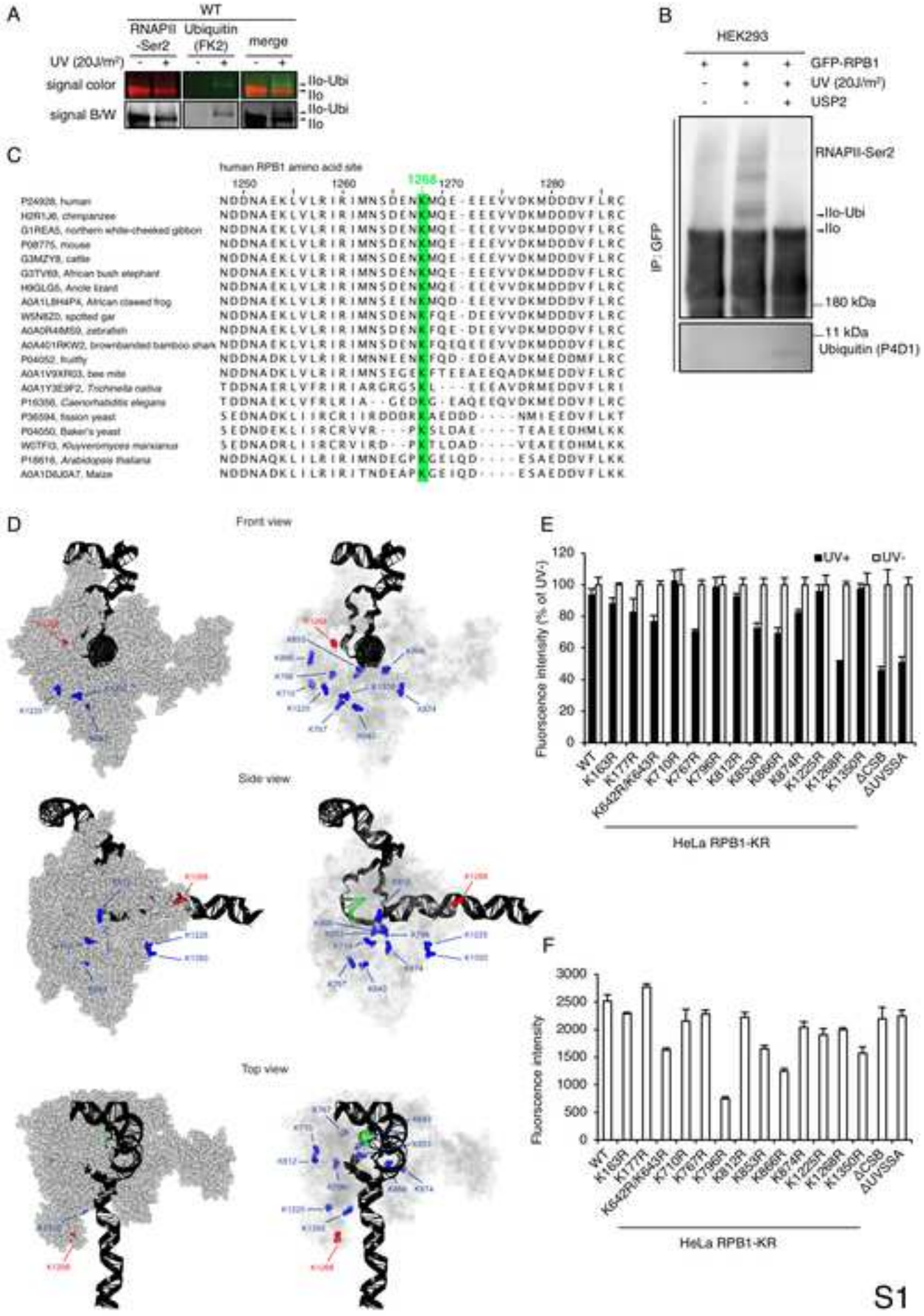

Supplemental Figure S2

Click here to access/download;Supplemental Figure;NakazawaFigS2R3.tiff

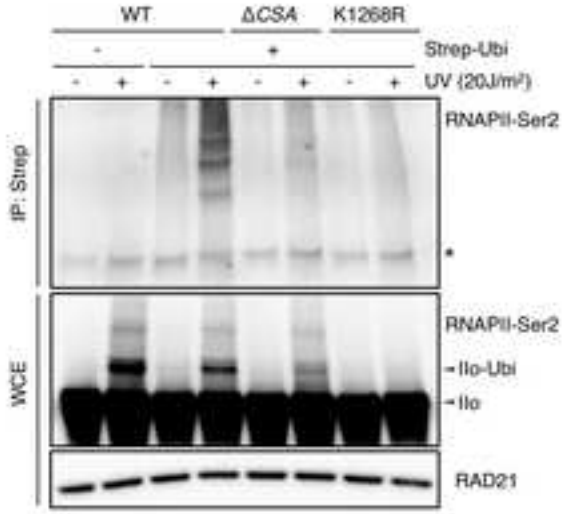

S2

Supplemental Figure S3

Click here to access/download;Supplemental Figure;NakazawaFigS3R3.tiff

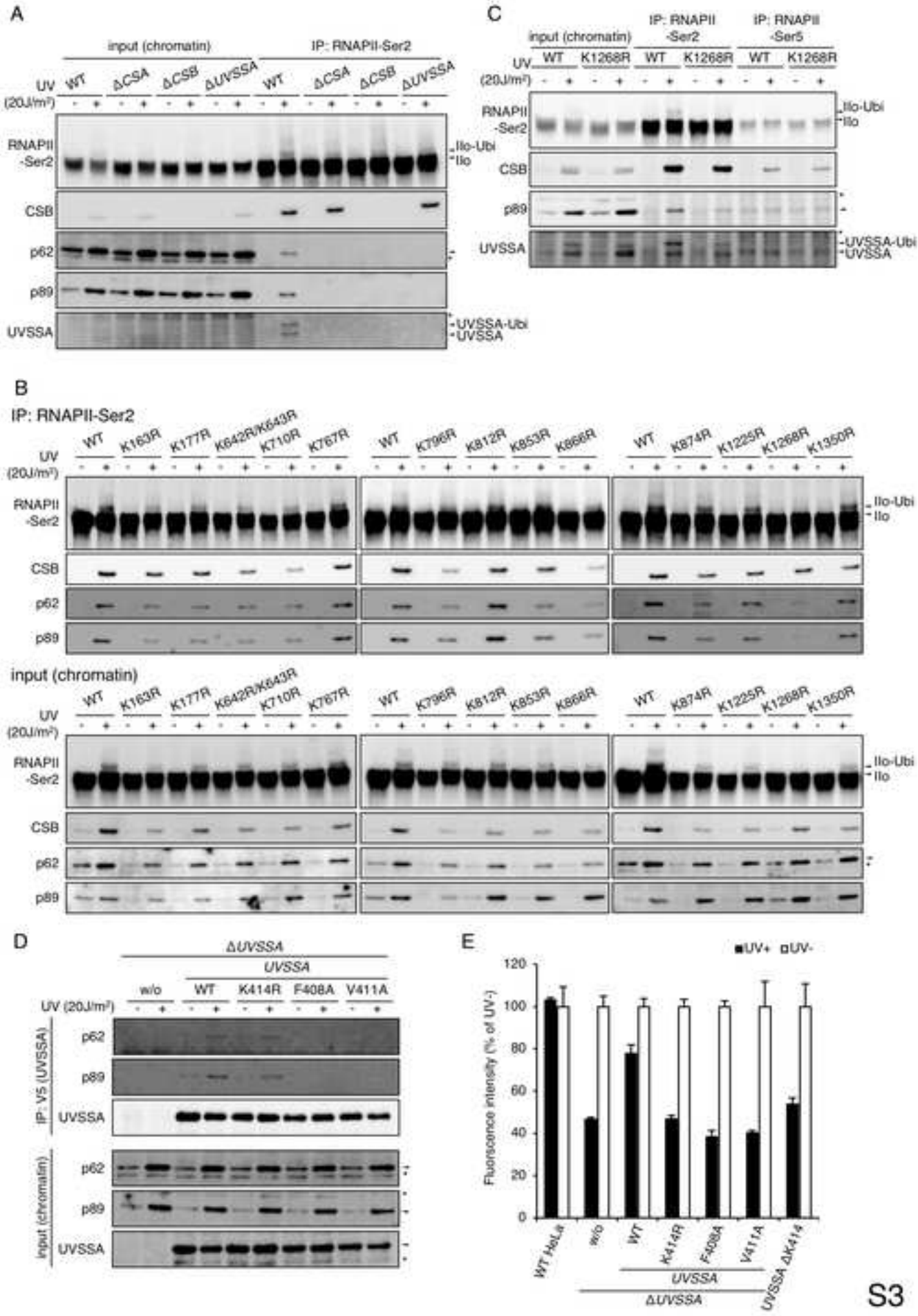

Supplemental Figure S4

Click here to access/download;Supplemental Figure;NakazawaFigS4R3.tiff

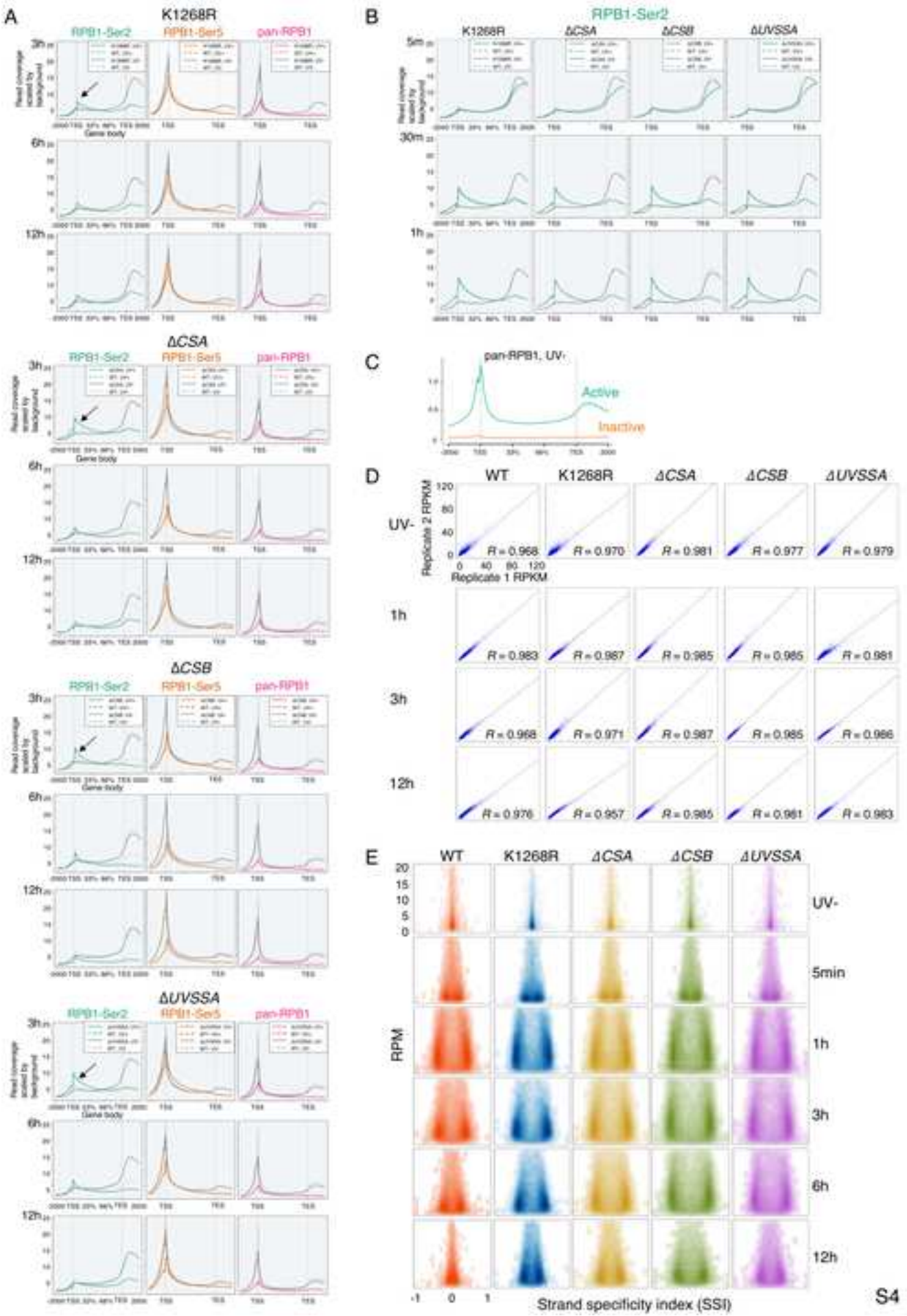

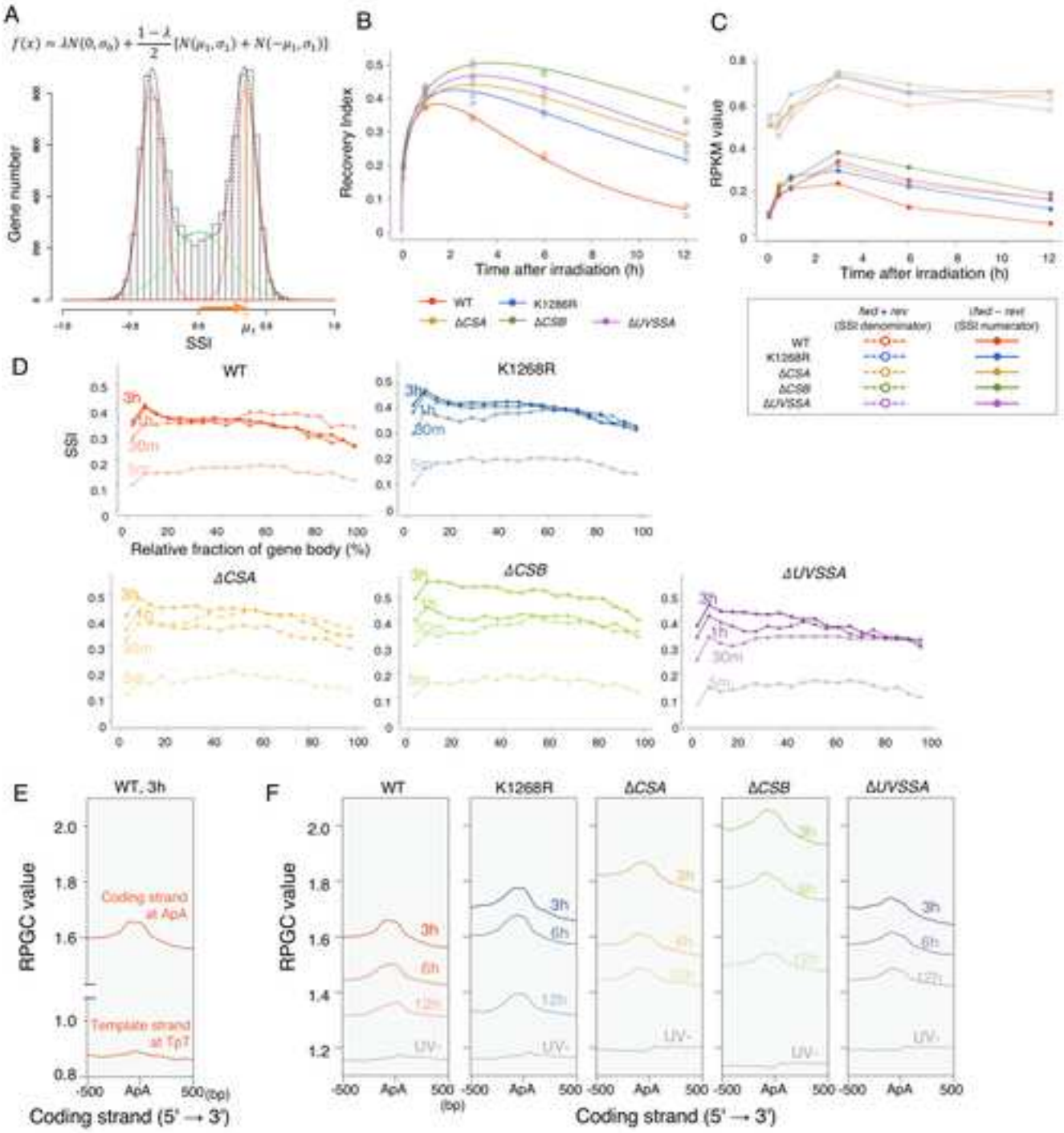

Click here to access/download;Supplemental Figure;NakazawaFigS6R3.tiff